A non-Gaussian Approach to Heavy Particle Simulation in Turbulent Flow

Thorsteinn Freygardsson

DEPARTMENT OF MATHEMATICS

CHALMERS UNIVERSITY OF TECHNOLOGY
Gothenburg, Sweden 2024
www.chalmers.se

Master's thesis 2024

Heavy Particle Simulation in Turbulent Flow

A non-Gaussian Approach

Thorsteinn Freygardsson

CHALMERS
UNIVERSITY OF TECHNOLOGY

Department of Mathematics
Chalmers University of Technology
Gothenburg, Sweden 2024

Heavy Particle Dynamics in Turbulent Flow
A non-Gaussian Approach
Thorsteinn Freygardsson

Supervisor: Kristian Gustafsson †
Co-supervisor: Bernhard Mehlig †
Examiner: Kristian Gustafsson †
†Department of Physics, University of Gothenburg

Master's Thesis 2024
Department of Mathematics
Chalmers University of Technology
SE-412 96 Gothenburg
Telephone +46 31 772 1000

Cover: Distribution of particles in highly persistent flow.

Typeset in LaTeX
Printed by Chalmers Reproservice
Gothenburg, Sweden 2024

Heavy Particle Simulation in Turbulent Flow
A non-Gaussian Approach
Thorsteinn Freygardsson
Department of Mathematics
Chalmers University of Technology

Abstract

The behaviour of heavy particles suspended in turbulence is of vital importance in many branches of science. It gives insight into droplet formation in clouds, plankton distribution in the oceans and pollen carried by the wind, among other things. Turbulent systems are highly dependent on the system parameters, making experimental observation and classical simulations difficult. However, statistical models of these systems can often give insight into the dynamics of suspended particles. In this thesis such a statistical model is constructed, and the dynamics of inertial particles in such a flow are analyzed. Our main focus is on how non-Gaussian flows affect preferential sampling, and we will also look into void formation and fractal clustering.

Keywords: Turbulence, Statistical Modelling, Inertial Particles, Preferential Sampling, Void Formation, Fractal Clustering.

Acknowledgements

I would like to offer my sincere gratitude to my supervisor, Kristian Gustafsson, and my co-supervisor, Bernhard Mehlig, without whom this thesis never would have come to fruition. Their insightful remarks and enthusiasm towards this research were critical to the success of this project.
I would also like to thank Alain Pumir and Javier Sierra-Ausin for their cooperation on the subject of void formation.
Finally, the computations were enabled by resources provided by Chalmers e-Commons at Chalmers.

Thorsteinn Freygardsson, Gothenburg, June 2024

List of Acronyms

Below is the list of acronyms that have been used throughout this thesis listed in alphabetical order:

DNS	Direct Numerical Simulation
ETD	Exponential Time Differencing
IF	Integrating Factor
RKX	Runge-Kutta of order X

Nomenclature

Below is the nomenclature of indices, sets, parameters, and variables that have been used throughout this thesis.

Parameters

γ	Stokes damping constant
τ_{p}	Timescale of particle interaction
τ_{f}	Timescale of flow correlations
τ_{η}	Kolmogorov timescale
ϕ	Stream function
$\mathbf{u}$	Flow velocity field
$\mathbb{A}$	Flow velocity gradient field
$\mathbb{S}$	Symmetric part of flow velocity gradient field
$\mathbb{O}$	Anti-symmetric part of flow velocity gradient field
l_{f}	Correlation length of the flow
St	Stokes number
Ku	Kubo number

Variables

$\mathbf{r}$	Spatial coordinate vector for particle position
$\mathbf{v}$	Particle velocities
$\mathbb{Z}$	Particle velocity gradients

Contents

List of Figures

1
Introduction

The transport of particles in turbulent flow is common in nature and in industry. It has applications ranging from explaining plankton distribution in the ocean [1] to chemical mixing in industrial settings [2] to facilitating droplet formation in clouds [3]. The transport of particles can be passive or active. Transport of non-organic matter is generally passive, but some microorganisms actively swim in the flow field. My thesis primarily focuses on the passive transport of particles.

Tracer particles are particles that follow the flow of the medium. They generally have similar mass density as that of the medium. Heavier particles, with mass density greater than that of the carrying medium, can detach from the flow. In an incompressible flow field, this leads to particles being more likely to sample some regions of the flow compared to others. This phenomenon is called preferential sampling, and is caused by the particles' inertia allowing them to spiral out of vortical regions [4]. One may also observe regions in the flow completely devoid of particles. These regions are called voids [3], and occur when vortices expel the particles out of that region. Finally, one may observe that particles form fractals in the flow. These fractals are statistically scale invariant, and show more and more structure as one zooms in or out [5].

A common method for numerical simulations in computational fluid dynamics is through direct numerical simulations (DNS) of the Navier-Stokes equations coupled with the particle dynamics. These simulations are costly, and in general only viable at small Reynolds numbers [5], $\mathrm{Re} = a|\mathbf{u} - \mathbf{v}|/\nu$, where a is the particle radius, $\mathbf{u}$ and $\mathbf{v}$ are the fluid velocity and particle velocity, respectively, and ν is the kinematic viscosity of the fluid. The Reynolds number can be thought of as a measure of the turbulence in a system, with higher Reynolds numbers indicating stronger turbulence.

Another method for numerical simulations is through statistical models. Specifically, by modelling the flow field through statistical models, one can then simulate the particle dynamics in that flow. Much of those dynamics is insensitive to the details of the flow. As for the flow itself, similar mechanisms are at play in flows with different Reynolds numbers (simulated using DNS) as in the statistical models. Still, some differences are observed. Firstly, particles with small inertia show a lower degree of preferential sampling in the statistical model compared to in the DNS. Secondly, the Gaussian model has difficulties simulating void formation, especially when vortices are strong but short lived. Thus, we ponder whether a better model could reconcile

Ask for clarification

these differences. We then arrive at the goal of this research. The goal of this research is to perform simulations using a non-Gaussian model with heavier tails than the Gaussian model, and with the aim to:

- Reconcile findings from DNS and Gaussian statistical simulations
- Measure the importance of the heavy tails in void formation
- If time allows, measure the impact of the heavy tails in fractal clustering

The outline of this thesis is as follow. Chapter 2 discusses the theory relevant to this thesis. We start with a discussion on the Navier-Stokes equations and statistical modelling, and the latter part of this chapter is on preferential sampling, void formation and fractal clustering. After that, chapter 3 discusses the methods utilised throughout this thesis. It includes a description of the statistical modelling, an interpolation scheme, a non-dimensionalisation scheme and an integration scheme for the equations of motion of the particles. Finally chapter 4 presents the results of this thesis and chapter 5 contains a discussion of the results as well as the conclusion of this thesis.

2
Theory

This chapter focuses on the theory relevant to this research. First we derive the fundamental equations governing the motion of fluids; the Navier-Stokes equations. They are used during DNS simulations, and are a good metric of comparison for the statistical models mentioned in chapter 1. The statistical models are discussed after the section on the Navier-Stokes equations, but the numerical implementation is delegated to chapter 3. Afterwards, we derive the equations of motion for small, heavy and spherical particles in a flow field. Then we derive quantities to measure preferential sampling and fractal clustering, allowing us to quantify our results and compare them to established literature. Finally, we model void formation and derive two formation mechanisms through a simple example.

2.1 The Velocity Field

Consider a fluid in some state of motion. A fluid velocity field is constructed such that for every point in some domain, it associates a velocity to the fluid at that point. A fluid velocity field must satisfy a set of conditions, which are encapsulated in the Navier-Stokes equations with suitable boundary conditions. Following the steps taken in [6, 7, 8], section 2.1.1 introduces some required concepts and derives the Navier-Stokes equations.

2.1.1 The Navier-Stokes Equations

The Navier-Stokes Equations consist of two equations. The first one describes the conservation of mass in a fluid system, whereas the second equation, often called the momentum equation, is derived from the conservation of momentum in the fluid system. They assume the fluid can be regarded as a continuum and that all fields of interest are weakly differentiable. To derive those equations we first need to introduce some quantities and relations.
First we define the material derivative. It is defined as

$$\frac{D}{Dt} \stackrel{\text{def}}{=} \frac{\partial}{\partial t} + \mathbf{u} \cdot \nabla \tag{2.1}$$

where the first term on the right hand side is a simple Eulerian derivative and describes the rate of change in a quantity at a fixed position and the second term is a directional derivative, i.e. it measures the rate of change of a quantity in the direction of $\mathbf{u}$ at the same fixed point. Thus the material derivative measures the changes in some quantity along a streamline in the velocity field $\mathbf{u}$.

The next thing we are interested in is continuity equations as the Navier-Stokes equations are derived based on the principle of conservation of mass and conservation of momentum, both of which can be formulated using a continuity equation. Assume we have some volume Ω with a boundary Γ. A continuity equation relates the rate of change of a quantity within Ω to the flow through the boundary Γ and the sources and sinks within Ω. A general form for such equations in differential form is

$$\frac{\partial \varphi}{\partial t} + \nabla \cdot (\varphi \mathbf{u}) = s \tag{2.2}$$

where φ is the density of the observed quantity, $\mathbf{u}$ is the flow velocity field and s quantifies the generation of the quantity in question per unit volume per unit time. It is a sum of generating terms, called sources, and destructive terms, called sinks. In the case where the observed quantity is conserved, there are no sources or sinks and as such $s = 0$.

2.1.1.1 Conservation of Mass

As mentioned, the first of the Navier-Stokes equations concerns the conservation of mass. Let ρ denote the mass density. Mass is assumed to be conserved in fluid flow which leads to the following form of the continuity equation:

$$\frac{\partial \rho}{\partial t} + \nabla \cdot (\rho \mathbf{u}) = 0 \tag{2.3}$$

This equation is one of the Navier-Stokes equations. If $\frac{D\rho}{Dt} = 0$, the fluid is incompressible since the rate of change of the density along streamlines is zero. In that case the equation simplifies to

$$\nabla \cdot \mathbf{u} = 0 \tag{2.4}$$

2.1.1.2 Conservation of Momentum

Now consider the conservation of momentum. The momentum density is given by $\rho\mathbf{u}$ which leads to a continuity equation of the form

$$\frac{\partial}{\partial t}(\rho \mathbf{u}) + \nabla \cdot (\rho \mathbf{u}\mathbf{u}) = \nabla \cdot \sigma + \rho \mathbf{f} \tag{2.5}$$

Here $\mathbf{uu}$ is a dyadic product, σ is a stress tensor and $\mathbf{f}$ represents forces acting throughout the body of the fluid, e.g. gravity. The divergence of a dyadic product is [9, 10]

$$\nabla \cdot (\mathbf{ab}) = (\nabla \cdot \mathbf{a})\mathbf{b} + \mathbf{a} \cdot \nabla \mathbf{b} \tag{2.6}$$

Thus we get

$$\rho \frac{\partial \mathbf{u}}{\partial t} + \mathbf{u}\frac{\partial \rho}{\partial t} + (\nabla \cdot \rho \mathbf{u})\mathbf{u} + \rho \mathbf{u} \cdot \nabla \mathbf{u} = \nabla \cdot \sigma + \rho \mathbf{f} \tag{2.7}$$

which leads to

$$\mathbf{u}\left(\frac{\partial \rho}{\partial t} + (\nabla \cdot \rho \mathbf{u})\right) + \rho\left(\frac{\partial \mathbf{u}}{\partial t} + \mathbf{u} \cdot \nabla \mathbf{u}\right) = \nabla \cdot \sigma + \rho \mathbf{f} \tag{2.8}$$

The first term on the left hand side is zero by mass conservation and the brackets in the second term denote the material derivative of $\mathbf{u}$. The resulting equation is

$$\rho \frac{D\mathbf{u}}{Dt} = \nabla \cdot \sigma + \rho \mathbf{f} \tag{2.9}$$

This is the second of the Navier-Stokes equations, though often, the stress tensor is expressed as a sum of a viscosity term and a pressure term. This relation can be written as $\sigma = -p\mathbf{I} + \boldsymbol{\tau}$ where p denotes the pressure and $\boldsymbol{\tau}$ is a measure of the viscosity.
Often one is interested in incompressible flow. Then one makes the assumption that the fluid is isotropic and the stress is Galilean invariant. With the added assumption of uniform viscosity, which implies $\nabla \cdot \boldsymbol{\tau} = \mu \nabla \cdot (\nabla \mathbf{u} + \nabla \mathbf{u}^T) = \mu \nabla^2 \mathbf{u}$, the Navier Stokes equations take the form

$$\nabla \cdot \mathbf{u} = 0 \tag{2.10a}$$

$$\frac{D\mathbf{u}}{Dt} = \nu \nabla^2 \mathbf{u} - \frac{1}{\rho} \nabla p + \mathbf{f} \tag{2.10b}$$

The variable ν is called the kinematic viscosity of the fluid, and is given by the ratio of the dynamic viscosity, μ, and the fluid density, ρ. The relation between $\boldsymbol{\tau}$ and μ is $\boldsymbol{\tau} = \mu \left[\nabla \mathbf{u} + (\nabla \mathbf{u})^T\right]$.

2.1.2 Statistical Modelling

Another common method for simulating a velocity field is through statistical models. A common method for generating a time-dependent incompressible random field is to evaluate it as a sum over time dependent Fourier coefficients [11, 5]. A newer approach uses such a method with time independent Fourier coefficients to make snapshots of the flow and then generates the time dependent flow as a superposition of the snapshots, weighted with random coefficients [12]. It is well known that for any vector $\mathbf{a}$ in three dimensions, the divergence of the curl of $\mathbf{a}$ is zero. Thus it is convenient to express the (incompressible) velocity in terms of the curl of a vector potential in 3 dimensions. In two dimensions the velocity is expressed in terms of partial derivatives of a potential. We call this potential the stream function and denote it by $\phi(\mathbf{r})$. The stream function is constructed from random Fourier modes to satisfy a given correlation relation. A superposition of such fields, with time dependent coefficients, then make up the time dependent velocity field. The details of the method are presented in chapter 3.

2.2 Particle Dynamics

The dynamics of particles suspended in fluid depend greatly on the properties of the particles themselves. The particles impose boundary conditions upon Eqs. (2.10). In particular, for solid particles, at any point on the surface the fluid velocity must equal the particle velocity. The force on such a particle has been evaluated. Maxey and Riley [13] denote this force the "Force from the unsteady Stokes Flow" and

calculate an approximation and Bec et al. [11] call it the hydrodynamic force. This force is given by the integral of the normal component of the stress tensor across the surface of the sphere, but perturbative methods are often used to find an expression for the force. Using such methods for a spherical particle with radius a and velocity $\mathbf{v}$ in a gravitational field $\mathbf{g}$ and neglecting the convection term in Eq. (2.10b) yields [11, 13]

$$\begin{aligned}\mathbf{F}_h &= \frac{4\pi}{3}\varrho_f a^3 \tfrac{D}{Dt}\mathbf{u}(\mathbf{r},t) - 6\pi\nu\varrho_f a[\mathbf{v}-\mathbf{u}(\mathbf{r},t)] \\ &\quad -\frac{4\pi}{3}\varrho_f a^3\mathbf{g} - \frac{2\pi}{3}\varrho_f a^3\frac{d}{dt}[\mathbf{v}-\mathbf{u}(\mathbf{r},t)] \\ &\quad -6\sqrt{\pi\nu}\varrho_f a^2\int_0^t \frac{ds}{\sqrt{t-s}}\frac{d}{ds}[\mathbf{v}-\mathbf{u}(\mathbf{r},s)] \end{aligned} \tag{2.11}$$

The variable ϱ_f denotes the fluid density and ν is the kinematic viscosity discussed above. An important distinction must be made between the two derivatives observed. The first, $\frac{D}{Dt}$, denotes the time derivative following a fluid element, and is qualitatively equal to the material derivative in section 2.1.1. The other derivative, $\frac{d}{dt}$, is the time derivative following a particle through the fluid, $\frac{d}{dt} = \frac{\partial}{\partial t} + \mathbf{v}\cdot\nabla$ [13]. The terms on the right hand side constitute, in order, the pressure-gradient force, Stokes' force, Archimedes' force, the added mass-force and the history force. The quality of this approximation is unclear, as several terms of order $\sim a^2$ and $\sim a^3$ have been neglected. However, Stokes' force, which we are most interested in scales as $\sim a$ and as such this approximation is still useful [11].

2.2.1 The Equations of Motion

From the prior section we find that for a small, spherical particle suspended in fluid flow and with density much greater than the fluid density, all terms on the right hand side of Eq. (2.11) are negligible except for Stokes' force. Writing the force as a product of mass and acceleration one arrives at the following equation of motion, neglecting gravitational effects

$$\dot{\mathbf{r}} = \mathbf{v} \tag{2.12a}$$

$$\dot{\mathbf{v}} = \frac{1}{\tau_\mathrm{p}}(\mathbf{u}-\mathbf{v}) \tag{2.12b}$$

The dots indicate time derivatives, $\mathbf{r} = \mathbf{r}(t)$ is the particle position at a given time, $\mathbf{u} = \mathbf{u}(\mathbf{r}(t),t)$ is the fluid velocity at the particle position at time t, $\mathbf{v} = \mathbf{v}(\mathbf{r}(t),t)$ is the particle velocity at the particle position at time t and τ_p is the Stokes time, $\tau_\mathrm{p} = m_p/6\pi\nu\varrho_f a$. Any gravitational effects are neglected which is justified if the particle size is small enough. In some cases the dynamics of the particle velocity gradients, $Z_{ij} = \partial v_i/\partial x_j$, are also important. Those dynamics can be obtained from Eq. (2.12), yielding the additional equation [5, 12]

$$\dot{\mathbb{Z}} = \frac{1}{\tau_\mathrm{p}}(\mathbb{A}-\mathbb{Z}) - \mathbb{Z}^2 \tag{2.12c}$$

2.3 Preferential Sampling

Preferential sampling refers to the tendency of particles to sample specific regions of the flow. In particular for heavy, spherical and inertial particles they tend to get ejected from vortical regions, aggregating in straining regions. For other types of particles, other mechanisms of preferential sampling exist, e.g. preferential sampling due to caustics. To characterise the preferential sampling for the heavy particles, it is convenient to introduce some notation. The fluid velocity gradients form a tensor, and are denoted as $\mathbb{A}$, $\mathbb{A} = \nabla \mathbf{u}$. These gradients can be decomposed into a symmetric part, $\mathbb{S} = (\mathbb{A} + \mathbb{A}^T)/2$, and an asymmetric part, $\mathbb{O} = (\mathbb{A} - \mathbb{A}^T)/2$. The symmetric and asymmetric contributions give information about the clustering of particles. The Stokes number St is a dimensionless measure of the particle inertia. It is defined as the ratio $St = \tau_\mathrm{p}/\tau_\eta$, where τ_η is the Kolmogorov time, $\tau_\eta = \sqrt{\nu/\varepsilon}$. Here $\varepsilon = \nu \mathrm{tr}\langle \mathbb{A}^T \mathbb{A} \rangle$ is the average kinetic energy dissipation rate.

2.3.1 Maxey's Centrifuge

Let us assume the absence of gravitational effects in which case Eq. (2.12) describes the motion of small, heavy, spherical particles in a fluid. We start by introducing $\mathbf{v}_p(\mathbf{r}(t), t)$ as a particle velocity field, valid for small Stokes number. A small value of St ensures the particle velocity field is single-valued everywhere; at higher values of St it becomes multi-valued due to caustics. By making an expansion at small Stokes number one obtains the following equation of motion [11, 4, 14]

$$\dot{\mathbf{r}} = v_p(\mathbf{r}, t) \approx \mathbf{u} - \tau_\mathrm{p} \frac{D}{Dt} \mathbf{u} \tag{2.13}$$

Taking the divergence of both sides we obtain

$$\nabla \cdot v_p(\mathbf{r}, t) = -\tau_\mathrm{p} \mathrm{tr} \mathbb{A}^2 \tag{2.14}$$

For tracer particles (i.e. particles that follow the flow lines) it is known that $\langle \mathrm{tr}\mathbb{A}^2 \rangle = 0$ in homogeneous flows. To see this, note that for homogeneous flows, the covariance $C(\mathbf{r}, \mathbf{r}') = \langle \mathbf{u}(\mathbf{r}) \mathbf{u}(\mathbf{r}') \rangle$ is only dependent on the separation between $\mathbf{r}$ and $\mathbf{r}'$, $C(\mathbf{r}, \mathbf{r}') = C(\mathbf{r} - \mathbf{r}')$. Utilising this along with incompressibility of the flow, $\partial_j u_j = 0$, we get (Note: implicit summation)

$$\begin{aligned}
& \langle \mathrm{tr}\mathbb{A}^2 \rangle \\
= \quad & \langle \partial_i u_j(\mathbf{r}) \partial'_j u_i(\mathbf{r}') \rangle \\
= \quad & \partial_i \partial'_j \langle u_j(\mathbf{r}) u_i(\mathbf{r}') \rangle \\
= \quad & \partial_i \partial'_j C_{ij}(\mathbf{r} - \mathbf{r}') \\
= \quad & -\partial_i \partial_j C_{ij}(\mathbf{r} - \mathbf{r}') \\
= \quad & -\langle \partial_i \partial_j u_j u_i \prime \rangle \\
= \quad & 0
\end{aligned}$$

However, Eq. (2.14) is concerned with the instantaneous velocity gradients, whose squared average can differ from zero. In regions with positive $\mathrm{tr}\mathbb{A}^2$ particles tend to move together whereas they tend to move apart where $\mathrm{tr}\mathbb{A}^2$ is negative. Note that $\mathrm{tr}\mathbb{A}^2$ can be decomposed as $\mathrm{tr}\mathbb{A}^2 = \mathrm{tr}\mathbb{S}\mathbb{S}^{\mathrm{T}} - \mathrm{tr}\mathbb{O}\mathbb{O}^{\mathrm{T}}$ where both terms are positive. This means that particles close to one another move together in regions where $\mathrm{tr}\mathbb{S}\mathbb{S}^{\mathrm{T}} > \mathrm{tr}\mathbb{O}\mathbb{O}^{\mathrm{T}}$ (straining regions) and move apart in regions where $\mathrm{tr}\mathbb{S}\mathbb{S}^{\mathrm{T}} < \mathrm{tr}\mathbb{O}\mathbb{O}^{\mathrm{T}}$. As a consequence there is a higher particle concentration in high-strain regions and lower concentration in low-strain regions which in turn leads to $\mathrm{tr}\langle\mathbb{A}^2\rangle$ measured at particle positions being higher for inertial particles than for tracer particles, i.e. the inertial particles preferentially sample high-strain regions.
Falkovich and Pumir [14] have estimated that along particle trajectories, and at small values of St, the relation $\mathrm{tr}\langle\mathbb{A}^2\rangle\tau_\eta^2 \sim \mathrm{St}$ holds. Here τ_η is the Kolmogorov timescale of the system, defined in section 2.3. However, direct numerical simulations (DNS) have shown that the scaling exponent seems to be smaller than the one given by the statistical models [11], which do scale as $\sim \mathrm{St}$. One of the aims of this project is to explain this difference.

2.4 Fractal Clustering

Fractal clustering refers to the fact that particles in compressible flow are not uniformly distributed in space but rather aggregate together, forming clusters. These fractal clusters are statistically scale invariant, showing more and more structure as one zooms either in or out. In general fractal clustering and preferential sampling do not imply one another, as we can have one without the other, but in the small St limit considered here, fractal clustering is caused by preferential sampling. This chapter starts with an introduction to Lyapunov exponents, which give information about the behaviour of closeby particles [15]. Next the Correlation dimension and the Lyapunov dimension, also called the Kaplan - Yorke dimension [16], are considered, but they can be used to quantify clustering.

2.4.1 Lyapunov Exponents

Lyapunov exponents of a dynamical system are a measure of the rate of separation of infinitesimally close trajectories in phase space. Indeed, let $\delta\mathbf{X}(t)$ denote the separation of two trajectories $\mathbf{X}_1, \mathbf{X}_2$ as a function of time, $\delta\mathbf{X}(t) = \mathbf{X}_1(t) - \mathbf{X}_2(t)$. Now assume that for large times and small initial separation $|\delta\mathbf{X}(0)|$ one gets asymptotically

$$|\delta\mathbf{X}(t)| \sim e^{\lambda t}|\delta\mathbf{X}(0)| \tag{2.15}$$

Then we call λ a Lyapunov exponent. If the Lyapunov exponent is positive then the separation is exponentially increasing, whereas if it is negative the separation is exponentially decreasing. In n-dimensional phase space we can have distinct separations along n different directions (other directions would be a linear combination of those n directions) and as such we can have n Lyapunov exponents. Thus we have a spectrum of Lyapunov exponents, whose total count is equal to the dimensionality of the space. The largest Lyapunov exponent is called the maximal Lyapunov

exponent and is an indicator of how chaotic the behaviour of dynamical systems are. The Lyapunov exponents are ordered in such a way that the largest is called the first (or maximal) Lyapunov exponent, the second largest the second Lyapunov exponent and so on,

$$\lambda_1 \geq \lambda_2 \geq \lambda_3 \geq \lambda_4 \geq \dots \tag{2.16}$$

Assuming we have a spectrum of n Lyapunov exponents, the sum of the m first Lyapunov exponents tells us about the behaviour of m-dimensional objects in n-space. For example $\lambda_1 + \lambda_2$ gives the exponential rate at which areas grow or shrink and $\lambda_1 + \lambda_2 + \lambda_3$ gives the exponential rate at which volumes change [17].

2.4.2 The Lyapunov Dimension

The Lyapunov dimension, also called the Kaplan-Yorke dimension, uses Lyapunov exponents to evaluate the dimension of an attractor, a (geometric) set of states in a dynamical system which the system tends to evolve towards. Let k be the index for which the sum of the first k Lyapunov exponents is non-negative and the sum of the first k + 1 Lyapunov exponents is negative:

$$\sum_{i=1}^{k} \lambda_i \geq 0 \tag{2.17}$$

$$\sum_{i=1}^{k+1} \lambda_i < 0 \tag{2.18}$$

Then the Lyapunov dimension is given by [16, 18, 19, 20]

$$d_L = k + \frac{1}{|\lambda_{k+1}|} \sum_{i=1}^{k} \lambda_i \tag{2.19}$$

For our purposes this dimension is equal to the information dimension of the system [21].

2.4.3 The Correlation Dimension

Similar to the Lyapunov dimension, the correlation dimension is a measure of the dimensionality of a system in space. It has the advantages of being straightforwardly and quickly calculated and working better when only a few points populate the space [21]. It is calculated as follows.
Assume we have a set of N points in m-dimensional space,

$$\mathbf{x}^{(i)} = [x_1^{(i)}, x_2^{(i)}, \dots, x_m^{(i)}],\ i = 1, 2, \dots, N. \tag{2.20}$$

These points can be used to calculate the correlation integral. The correlation integral measures the closeness of points and is given by

$$C(\varepsilon) = \lim_{N\to\infty} \frac{1}{N^2} \sum_{i,j=1}^{N} \Theta(\varepsilon - ||\mathbf{x}^{(i)} - \mathbf{x}^{(j)}||) \tag{2.21}$$

where ε is a reference distance, $||\cdot||$ is some norm and $\Theta(\cdot)$ is the Heaviside function. In Euclidean space using the Euclidean norm is common. As N tends to infinity, for small values of ε, we get an exponential relation for the correlation integral:

$$C(\varepsilon) \sim \varepsilon^{\kappa}. \tag{2.22}$$

Here κ is the correlation dimension. Thus as long as N is large enough one can obtain an estimate of κ by graphing $C(\varepsilon)$ against ε on a log-log graph.

2.5 Void Formation

This next section considers the formation of voids in turbulent environments. Such phenomena have been observed experimentally [3], and numerically [14, 22]. The inspiration for this section comes from a talk given by prof. Alain Pumir [23], which my co-supervisor, Bernhard Mehlig, attended. The following theory, and more so, the corresponding results, were obtained from a collaboration with prof. Alain Pumir and his PhD student, Javier Sierra-Ausin (Manuscript in preparation (2024)).
Consider the dynamics governed by Eqs. (2.12) at small values of St. We are interested in how the local particle density $n(\mathbf{r}, t)$ evolves. Its equation of motion stems from the Lagrangian continuity law ($\frac{d\varphi}{dt} + \varphi\nabla \cdot \mathbf{v} = 0$) for the particle density $n(\mathbf{r}, t)$ and is written as follows [14]

$$\frac{d}{dt}n(\mathbf{r}, t) = -\mathrm{tr}\mathbb{Z}(t)n(\mathbf{r}, t). \tag{2.23}$$

Integrating this differential equation from $t = -T$ to $t = 0$ along a Lagrangian trajectory we arrive at the solution

$$n_0 = n_{-T}\exp\left[-\int_{-T}^{0} \mathrm{tr}\mathbb{Z}(\mathbf{r}, t)dt\right]. \tag{2.24}$$

Here $\mathbb{Z}$ is the particle velocity gradient matrix introduced in section 2.2.1. Eq. (2.14) shows that for small Stokes numbers $\mathrm{tr}\mathbb{Z} \sim -\tau_{\mathrm{p}}\mathrm{tr}\mathbb{A}^2$. This results in Eq. (2) in [14]

$$n_0 = n_{-T}\exp\left[\tau_{\mathrm{p}}\int_{-T}^{0} \mathrm{tr}\mathbb{A}^2(\mathbf{r}, t)dt\right]. \tag{2.25}$$

Eq (2.24) shows that the particle density will be small where the history of $\mathrm{tr}\mathbb{Z}$ is large and positive. Equivalently, Eq. (2.25) states that the particle density will be small where the history of $\mathrm{tr}\mathbb{A}^2$ will be large and negative. In section 2.3.1 we saw that $\mathrm{tr}\mathbb{A}^2$ could be decomposed as $\mathrm{tr}\mathbb{A}^2 = \mathrm{tr}\mathbb{S}\mathbb{S}^T - \mathrm{tr}\mathbb{O}\mathbb{O}^T$, which means the requirement for a small particle density is that trajectories cross vortical regions in the past (i.e. $\mathrm{tr}\mathbb{O}\mathbb{O}^T$ is large). Note that the history depends on the instantaneous value of $\mathrm{tr}\mathbb{A}^2$ and as such, even at small St, the integral can be large and voids can form. We have identified two main mechanisms that can cause the integral to become very large

1. A persistent vortex of moderate strength expels particles
2. A short lived vortex of great strength expels particles

These two cases are fundamentally different, as will be hinted at in the following simple problem.

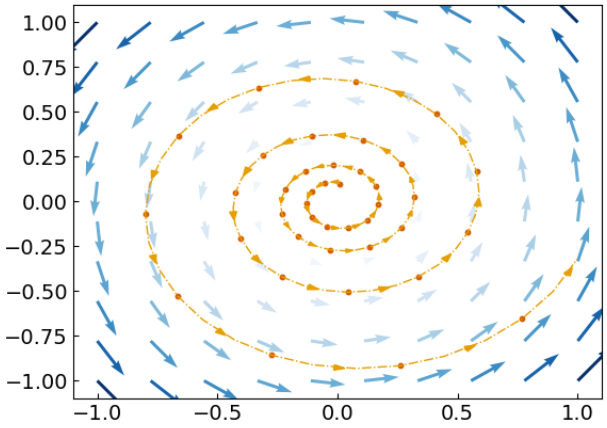

Figure 2.1: The vortex described by the velocity gradient field (2.26). Also shown is a particle following the dynamics (2.27).

2.5.1 A Simple Problem

We assume we have a two-dimensional vortex

$$\mathbb{A} \sim \mathbb{O} = \begin{bmatrix} 0 & -\Omega \\ \Omega & 0 \end{bmatrix}, \tag{2.26}$$

with Ω the vorticity, $\Omega = \frac{1}{2}\varepsilon_{3jk}A_{kj}$. The dynamics of particles in such a vortex are given by

$$\frac{d}{dt}\mathbf{r} = \mathbf{v} \tag{2.27a}$$

$$\frac{d}{dt}\mathbf{v} = \frac{1}{\tau_\mathrm{p}}[\mathbb{A}\mathbf{r} - \mathbf{v}] \tag{2.27b}$$

To get a clearer picture, we look at figure 2.1. It shows the vortex described by Eq. (2.26) and the dynamics of an inertial particle in that vortex. The particle is initially close to the center of the vortex but slowly spirals out.
On matrix form the dynamics give a matrix differential equation, $\dot{\mathbf{W}} = \mathbb{C}\mathbf{W}$ with $\mathbf{W} = (r_1, r_2, v_1, v_2)$ and

$$\mathbb{C} = \begin{bmatrix} 0 & \mathbb{I} \\ \mathbb{A}/\tau_\mathrm{p} & -\mathbb{I}/\tau_\mathrm{p} \end{bmatrix}. \tag{2.28}$$

The eigenvalues of $\mathbb{C}$ are the Lyapunov exponents of the system. The product of the maximal Lyapunov exponent and the correlation time of the vortex ($\sim$ lifetime of the vortex) will dictate whether a void can be formed. The eigenvalues of matrix (2.28) are

$$\Lambda = \frac{1}{2\tau_\mathrm{p}}\left[-1 \pm \sqrt{1 \pm \mathrm{i}4\Omega\tau_\mathrm{p}}\right]. \tag{2.29}$$

These eigenvalues form complex pairs. In total there are two such pairs, one which has a positive real part. That pair determines the maximal Lyapunov exponent.

For $\Omega > 0$ one gets (obtained via the software Maple)

$$\lambda_{\max} = \frac{1}{2\tau_\mathrm{p}}\left[-1+\sqrt{\tfrac{1}{2}\sqrt{1+(4\Omega\tau_\mathrm{p})^2}+\tfrac{1}{2}}\right] \sim \begin{cases} \Omega^2\tau_\mathrm{p} & \Omega\tau_\mathrm{p} \ll 1\,, \\ \sqrt{\Omega/2\tau_\mathrm{p}} & \Omega\tau_\mathrm{p} \gg 1\,. \end{cases} \tag{2.30}$$

We now consider two cases and match them to the expressions in Eq. (2.30). First, a persistent flow with large $\mathrm{Ku} = \tau_\mathrm{f}\mathrm{u}_0/\mathrm{l}_\mathrm{f}$ and small $\mathrm{St} = \tau_\mathrm{p}/\tau_\eta$ has typical fluctuations $\Omega \sim \tau_\eta^{-1}$ and corresponds to the first case in Eq. (2.30). This yields the criterion $\lambda_{\max}\tau_\mathrm{f} \sim (\tau_\mathrm{p}/\tau_\eta^2)\tau_\mathrm{f} \gg 1$ for void formation, or, since $\tau_\eta \sim l_\mathrm{f}/u_0$,

$$\mathrm{StKu} \gg 1. \tag{2.31a}$$

Secondly, we look at anomalously large values of Ω, which corresponds to the second case in Eq. (2.30). Then for void formation the following two conditions must be satisfied, $\Omega\tau_\mathrm{p} \gg 1$ and $\tau_\mathrm{f}\sqrt{\Omega/\tau_\mathrm{p}} \gg 1$, which can also be written as

$$\Omega\tau_\eta \gg \mathrm{St}^{-1} \quad \text{and} \quad \Omega\tau_\eta \gg \mathrm{St}/\mathrm{Ku}^2. \tag{2.31b}$$

In general the first condition is more restrictive, only when $\mathrm{Ku} \to 0$, the so called white noise limit, does the second condition come into play.

3
Methods

This chapter focuses on the methods utilised during the course of this project. We start with a discussion about the statistical model used, then we move onto the interpolation scheme used for the particle dynamics. Afterwards we look at the non-dimensionalisation scheme we used for the equations of motion and finally we look at the integration method used for some of the results.

3.1 Statistical Modelling

As was mentioned in chapter 2 this section contains a more detailed discussion of the statistical model used in simulations. We first take a look at the time-independent model and then at how time dependence is implemented [12].

3.1.1 Time-Independent Flow

All flow components are characterised in terms of derivatives of a stream function or a vector potential. The velocity can then be expressed as

$$\mathbf{u} = \begin{pmatrix} \partial_y \phi(\mathbf{r}) \\ -\partial_x \phi(\mathbf{r}) \end{pmatrix} \qquad \text{in 2d} \tag{3.1}$$

$$\mathbf{u} = \nabla \times \mathbf{A}(\mathbf{r}) \qquad \text{in 3d} \tag{3.2}$$

where $\phi(\mathbf{r})$ is a stream function and $\mathbf{A}$ is a vector potential with components A_1, A_2 and A_3. The functions ϕ, A_1, A_2, A_3 are independent Gaussian random functions. Hereafter we will only consider ϕ but the same methods apply for A_1, A_2 and A_3. Similar to the velocity we can obtain an expression for the velocity gradients. In 2D we obtain:

$$A = \begin{pmatrix} \frac{\partial u_1}{\partial x} & \frac{\partial u_1}{\partial y} \\ \frac{\partial u_2}{\partial x} & \frac{\partial u_2}{\partial y} \end{pmatrix} = \begin{pmatrix} \partial_x \partial_y \phi(\mathbf{r}) & \partial_y^2 \phi(\mathbf{r}) \\ -\partial_x^2 \phi(\mathbf{r}) & -\partial_x \partial_y \phi(\mathbf{r}) \end{pmatrix} \tag{3.3}$$

We use a Gaussian stream function and as such it is completely characterised by its mean and covariance. The mean is assumed to be zero and a Gaussian spatial covariance is assumed;

$$\langle \phi(\mathbf{r}) \rangle = 0 \tag{3.4a}$$

$$\langle \phi(\mathbf{r}) \phi(\mathbf{r}') \rangle = \frac{l_\mathrm{f}^2 u_0^2}{d(d-1)} e^{-\frac{|\mathbf{r}-\mathbf{r}'|^2}{2l_\mathrm{f}^2}} \tag{3.4b}$$

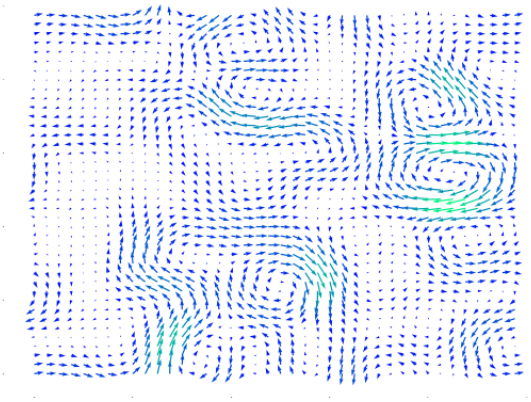

Figure 3.1: An example flow snapshot from the procedure in section 3.1.1.

Here l_f is the correlation length of the flow, u_0 is a typical speed of the flow and d denotes the number of dimensions. Eq. (3.4) only depends on the magnitude of the separation between $\mathbf{r}$ and $\mathbf{r}'$, and as such ensures the flow is isotropic and homogeneous in space. Constructing the stream function in terms of Fourier modes with random coefficients yields the desired statistical relation in Eq. (3.4)

$$\phi(\mathbf{r}) = (2\pi)^{\frac{d}{4}} \frac{l_\mathrm{f}^{d/2+1} u_0}{\sqrt{V_d d(d-1)}} \sum_{\mathbf{k}} a_{\mathbf{k}} e^{i\mathbf{k}\cdot\mathbf{r} - \frac{k^2 l_\mathrm{f}^2}{4}} \tag{3.5}$$

Here V_d is the system volume, $V_d = L_x L_y L_z$ in three dimensions and $V_d = L_x L_y$ in two dimensions. L_x, L_y and L_z are the system sizes in the x-, y- and z-direction. Additionally $\mathbf{k}$ is a wave vector, $\mathbf{k} = 2\pi(n_x/L_x, n_y/L_y)$ in 2d, with n_x, n_y integers between $-\frac{2L_x}{l_\mathrm{f}}, \ldots, \frac{2L_x}{l_\mathrm{f}}$ and $-\frac{2L_y}{l_\mathrm{f}}, \ldots, \frac{2L_y}{l_\mathrm{f}}$ respectively. In order for the covarianve in Eq. (3.4) to hold, we must demand that $L_x, L_y \gg l_\mathrm{f}$. The Fourier coefficients $a_{\mathbf{k}}$ are zero mean Gaussian random numbers with covariance $\langle a_{\mathbf{k}} a_{\mathbf{k}'} \rangle = \delta_{\mathbf{k}\mathbf{k}'}$ and must also satisfy $a^*_{\mathbf{k}} = a_{-\mathbf{k}}$ so that the sum in Eq. (3.5) is real [5]. Figure 3.1 shows an example of a flow snapshot generated by this procedure.

3.1.2 Time Dependence

To generate a time dependent velocity field we randomly select M different flow snapshots, generated by the procedure in section 3.1.1, and write the time dependent field as a superposition of them;

$$\mathbf{u}(\mathbf{r}, t) = \sum_{m=1}^{M} C_m(t) \mathbf{u}^{(m)}(\mathbf{r}) \tag{3.6}$$

The coefficients $C_m(t)$ are independent zero mean Gaussian random variables with covariance

$$\langle C_m(t) C_{m'}(t') \rangle = \frac{1}{M} \delta_{mm'} e^{-|t-t'|/\tau_\mathrm{f}} \tag{3.7}$$

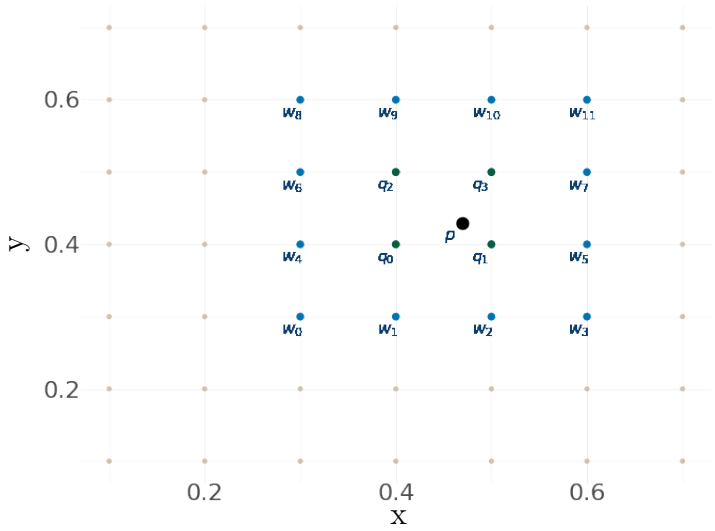

Figure 3.2: The interpolation setup. Here p is the point where we want to interpolate the function value, while q_i and w_j show the closest surrounding grid points, $i = 0, 1, 2, 3$ and $j = 0, 1, \ldots, 11$.

where τ_f is the time scale of the covariance. With this construction the time dependent potentials $\phi(\mathbf{r}, t)$ have covariance function

$$\langle \phi(\mathbf{r}, t)\phi(\mathbf{r}', t')\rangle = \frac{l_\mathrm{f}^2 u_0^2}{d(d-1)} e^{-\frac{|\mathbf{r}-\mathbf{r}'|^2}{2l_\mathrm{f}^2} - \frac{|t-t'|}{\tau_\mathrm{f}}} \tag{3.8}$$

Since the time covariance is exponential it is simple to use an Ornstein-Uhlenbeck process to generate the coefficients for different times [5, 24]. The following update scheme is used

$$C_m(t + \delta t) = e^{-\frac{\delta t}{\tau_\mathrm{f}}} C_m(t) + B_m(t) \tag{3.9}$$

where B_m are independent zero mean Gaussian random variables with covariance $\langle B_m B_{m'}\rangle = \frac{1}{M}(1 - e^{-2\frac{\delta t}{\tau_\mathrm{f}}})\delta_{mm'}$.

3.2 Interpolation

A bicubic interpolation scheme[25] is used when intermediate velocity and gradient values are required in the particle dynamics. The flow snapshots from section 3.1.1 are precalculated and stored to a disk. They consist of a grid of discrete points where the velocity and velocity gradients are evaluated. For a general point p in that domain, the surrounding grid points can be used to calculate an estimate for the value at that point. Bicubic interpolation uses a total of 16 grid points to make such an estimate, the 4 closest nodes we denote q_0, q_1, q_2 and q_3, and the second closest nodes we denote $w_0, w_1, \ldots, w_{11}$. This setup is shown in Figure 3.2.
Assume we have a grid with spacing $\Delta x = \Delta y$. Let x and y denote the x- and y-coordinates of some point in the domain and let $q_0 = (x_0, y_0)$ denote the closest grid point with $x_0 \leq x$ and $y_0 \leq y$. We calculate the normalised interpolation coordinates $\bar{x} = \frac{x-x_0}{\Delta x}$ and $\bar{y} = \frac{y-y_0}{\Delta y}$. When expressed in terms of these normalised coordinates the interpolation problem has been mapped to the unit square.

We approximate $f(\bar{x}, \bar{y})$ with an interpolating surface

$$g(\bar{x}, \bar{y}) = \sum_{i=0}^{3} \sum_{j=0}^{3} a_{ij} \bar{x}^i \bar{y}^j \tag{3.10}$$

This equation has 16 unknown coefficients a_{ij}. Calculating the derivatives gives

$$g_x(\bar{x}, \bar{y}) = \frac{1}{\Delta x} \sum_{i=0}^{3} \sum_{j=0}^{3} a_{ij} i \bar{x}^{i-1} \bar{y}^j \tag{3.11}$$

$$g_y(\bar{x}, \bar{y}) = \frac{1}{\Delta y} \sum_{i=0}^{3} \sum_{j=0}^{3} a_{ij} j \bar{x}^i \bar{y}^{j-1} \tag{3.12}$$

$$g_{xy}(\bar{x}, \bar{y}) = \frac{1}{\Delta x \Delta y} \sum_{i=0}^{3} \sum_{j=0}^{3} a_{ij} i j \bar{x}^{i-1} \bar{y}^{j-1} \tag{3.13}$$

Calculating each of these quantities at (0, 0), (0, 1), (1, 0) and (1, 1) gives us 16 equations for 16 unknowns. This can be expressed as a matrix equation $\mathbb{A}\alpha = \mathbf{x}$ with

$$\begin{aligned} \alpha &= [a_{00}, a_{01}, a_{02}, a_{03}, a_{10}, \ldots, a_{33}] \\ \mathbf{x} &= [f(0,0), f(0,1), f(1,0) f(1,1), \Delta x f_x(0,0), \ldots, \Delta x \Delta y f_{xy}(1,1)] \end{aligned}$$

The function values at the node points are known, and can be used to approximate the derivatives. For example $\Delta x f_x(q_0) \approx (f(q_1) - f(w_4))/2$ and $\Delta x \Delta y f_{xy}(q_0) \approx (\Delta x f_x(q_2) - \Delta x f_x(w_1))/2 \approx ((f(q_3) - f(w_6)) - (f(w_2) - f(w_0)))/4$. Finally the coefficients are found by $\alpha = \mathbb{A}^{-1}\mathbf{x}$.

3.3 Non-Dimensionalisation

The equations of motion are put on a non-dimensional form. There are two main reasons for this. The first is that normalising the equations in such a way could lower the variation in the values that appear, thus making numerical calculations more stable. The second reason is that we want to combine the equations of motion, Eq. (2.12), into a single matrix equation for exponential integration (see section 3.4). However, with matrix entries having units, many operations, such as the matrix exponent, lose meaning. The non-dimensionalisation is done as follows.
First we note from section 2.3 that the Kolmogorov timescale is defined as $\tau_\eta = 1/\sqrt{\langle \mathrm{tr}\mathbb{A}\mathbb{A}^T \rangle}$. Noting that $\mathrm{tr}\mathbb{A}\mathbb{A}^T = 2a_{11}^2 + a_{12}^2 + a_{21}^2$, and thus $\langle \mathrm{tr}\mathbb{A}\mathbb{A}^T \rangle = 2\langle a_{11}^2 \rangle + \langle a_{12}^2 \rangle + \langle a_{21}^2 \rangle$, we can use Eqs. (3.3) and (3.4b) to calculate $\langle a_{11}^2 \rangle$, $\langle a_{12}^2 \rangle$ and $\langle a_{21}^2 \rangle$. Doing so we find that

$$\tau_\eta = \frac{l_\mathrm{f}}{2u_0} \tag{3.14}$$

with l_f the correlation length and u_0 a characteristic flow velocity as before. This allows us to define new dimensionless variables. We use the Kolmogorov time as

a characteristic time scale of the system and l_f as a characteristic length scale to define the following dimensionless variables.

$$t' = \frac{t}{\tau_\eta} \qquad \mathbf{r}' = \frac{\mathbf{r}}{l_\mathrm{f}} \tag{3.15}$$

$$\mathbf{v}' = \mathbf{v}\frac{\tau_\eta}{l_\mathrm{f}} \qquad \mathbf{u}' = \mathbf{u}\frac{\tau_\eta}{l_\mathrm{f}} \tag{3.16}$$

This, together with the definition of the Stokes number in section 2.3, leads us to the dimensionless equations of motion:

$$\dot{\mathbf{r}}' = \mathbf{v}' \tag{3.17a}$$

$$\dot{\mathbf{v}}' = \frac{1}{\mathrm{St}}(\mathbf{u}' - \mathbf{v}') \tag{3.17b}$$

This formulation also poses a slight change to the analysis presented in sections 3.1.1 and 3.1.2. For the velocity and the velocity gradients the non-dimensionalisation is done post-calculation. After generating the velocities and velocity gradients, the dimensionless variants are calculated according $\mathbf{u}' = \mathbf{u}\frac{\tau_\eta}{l_\mathrm{f}} = \mathbf{u}\frac{1}{2u_0}$ and $\mathbb{A}' = \mathbb{A}\tau_\eta = \mathbb{A}\frac{l_\mathrm{f}}{2u_0}$.
To deal with the time dependence we define a dimensionless parameter called the Kubo number, $\mathrm{Ku} = \frac{\tau_\mathrm{f} u_0}{l_\mathrm{f}}$. This leads to a correlation relation

$$\langle C_m(t_1')C_{m'}(t_2')\rangle = \frac{1}{M}\delta_{mm'}e^{-|t_1'-t_2'|/(2\mathrm{Ku})} \tag{3.18}$$

for the coefficients and an update rule

$$C_m(t' + \delta t') = e^{-\delta t'/(2\mathrm{Ku})}C_m(t') + B_m(t') \tag{3.19}$$

with B_m independent zero mean Gaussian random variables with covariance $\langle B_m B_{m'}\rangle = \frac{1}{M}(1 - e^{-\delta t'/\mathrm{Ku}})\delta_{mm'}$.

3.4 Exponential Integration

3.4.1 Introduction

Exponential integration is an explicit integration technique often helpful when solving stiff differential equations, as is the case for Eq. (3.17) in the small St limit. As such we hope to compare this method to other explicit methods, and determine whether it can resolve the particle dynamics better. Consider an initial value problem in one dimension

$$\dot{u}(t) = cu(t) + F(u,t) \tag{3.20a}$$

$$u(0) = u_0 \tag{3.20b}$$

We assume c is composed of linear terms and $F(u,t)$ of nonlinear terms (for our purposes we can think of c as constant). A common method for solving such an equation is to multiply each side of the equation by an integrating factor e^{-ct} to get

$$e^{-ct}F(u,t) = -e^{-ct}cu(t) + e^{-ct}\dot{u}(t) = \frac{d}{dt}(e^{-ct}u(t)) \tag{3.21}$$

Then integrating both sides from 0 to t followed by multiplication by e^{ct} yields

$$u(t) = e^{ct}u_0 + \int_0^t e^{c(t-\tau)}F(u(\tau),\tau)d\tau \tag{3.22}$$

Even for a system of differential equations with the corresponding initial conditions, one can write a matrix differential equation, separate the linear and nonlinear terms and arrive at a similar expression as Eq. (3.22).

3.4.2 Integrating Factor Methods

There are two main methods to construct a numerical scheme from Eqs. (3.21) and (3.22). The first one, called the integrating factor (IF) method, applies a numerical method (such as explicit Euler) directly to Eq. (3.21) to get an update scheme [26]. For example, setting $z(t) = e^{-ct}u(t)$ and $g(u,t) = e^{-ct}F(u,t)$, Eq. (3.21) reads

$$\frac{d}{dt}z = g(u,t)$$

With timestep h the explicit Euler method then gives

$$\begin{aligned} & z_{n+1} &&= && z_n + hg(u,t) \\ \iff \quad & e^{-ct_{n+1}}u_{n+1} &&= && e^{-ct_n}u_n + he^{-ct_n}F(u_n,t_n) \\ \iff \quad & u_{n+1} &&= && e^{ch}(u_n + hF_n) \end{aligned} \tag{3.23}$$

with $F_n \overset{\text{def}}{=} F(u_n,t_n)$. Eq. (3.23) is then the update scheme in the integrating factor explicit Euler scheme.

3.4.3 Exponential Time Differencing Methods

The second method is called exponential time differencing (ETD) [26]. It makes an approximation of $F(u(\tau),\tau)$ in Eq. (3.22). The simplest approximation is $F(u(\tau),\tau) = F_n$. The resulting update scheme is

$$u_{n+1} = e^{ch}u_n + \frac{e^{ch}-1}{c}F_n \tag{3.24}$$

These methods can also be used with multi-step methods such as the Runge-Kutta method. An example of a second order exponential time differencing Runge-Kutta method takes $F = F_n$ during the first step, calculating an intermediate state u_m, and then uses a linear approximation for F in τ during the second step: $F = F_n + \tau(F_m - F_n)/(h/2)$. The resulting update scheme is [26]

$$u_m = e^{ch/2}u_n + \frac{e^{ch/2}-1}{c}F_n \tag{3.25a}$$

$$u_{n+1} = e^{ch}u_n + \frac{e^{ch}-1}{c}F_n + 2\frac{e^{ch}-1-ch}{c^2h}(F_m - F_n) \tag{3.25b}$$

The update scheme used in this project is a fourth order exponential time differencing Runge-Kutta scheme derived by Cox and Matthews [27]. It is defined as follows:

$$
\begin{aligned}
a_n &= u_n e^{ch/2} + \frac{e^{ch/2}-1}{c} F_n && \text{(3.26a)}\\
b_n &= u_n e^{ch/2} + \frac{e^{ch/2}-1}{c} F(a_n, t_n + h/2) && \text{(3.26b)}\\
c_n &= a_n e^{ch/2} + \frac{e^{ch/2}-1}{c} (2F(b_n, t_n + h/2) - F_n) && \text{(3.26c)}\\
u_{n+1} &= u_n e^{ch} + \frac{1}{h^2 c^3}\{F_n[-4 - hc + e^{ch}(4 - 3hc + h^2c^2)] \\
&\quad 2(F(a_n, t_n + h/2) + F(b_n, t_n + h/2))[2 + hc + e^{ch}(-2 + hc)] \\
&\quad F(c_n, t_n + h)[-4 - 3hc - h^2c^2 + e^{ch}(4 - hc)]\} && \text{(3.26d)}
\end{aligned}
$$

We have verified that the original fourth order Runge-Kutta method can be recovered from this method by assuming h is small and making up to a third order Taylor expansion of the exponents around zero. In the case of a matrix equation care must be taken. Firstly, the division by c would no longer be possible, instead left multiplication by the inverse should be used. Secondly the square brackets in Eq. (3.26d) contain both scalar and matrix terms. To deal with this one should treat each scalar term as if it is multiplied by the identity matrix.

3.4.4 Scaling and Squaring

When c is close to 0 in the scalar equation, or when the eigenvalues of the corresponding matrix in the matrix equation are close to zero, the factor on the form

$$\varphi_1(\mathbb{B}) = \mathbb{B}^{-1}(e^{\mathbb{B}} - \mathbb{I}) \tag{3.27}$$

becomes difficult to calculate [28]. Here $\mathbb{I}$ is the identity matrix in n-dimensions. A scaling and squaring method based on Padé approximation has been suggested [29, 30] and shown to give a good approximation of the function value when an eigenvalue of $\mathbf{z}$ is close to zero [29, 31]. The method is as follows

1. Find the smallest $p \in \mathbb{Z}$ such that $2^p \geq ||\mathbb{B}||_\infty$
2. Scale the matrix $\mathbb{B}$: $\mathbb{B}_{sc} = \frac{1}{2^{max[0,p+1]}}\mathbb{B}$
3. Compute the Padé approximation
4. Undo the scaling

The details of the Padé approximation and how the scaling is undone are the subjects of the next two sections.

3.4.4.1 The Padé Approximation

The φ_1 function belongs to a family of similar functions. Defining $\varphi_0(\mathbb{B}) = e^{\mathbb{B}}$ this family obeys the recurrence relation [29]

$$\varphi_l(\mathbb{B}) = \mathbb{B}^{-1}\left(\varphi_{l-1}(\mathbb{B}) - \frac{\mathbb{I}}{(l-1)!}\right), \quad \varphi_l(\mathbf{0}) = \tfrac{\mathbb{I}}{l!}, \quad l = 1, 2, \ldots \tag{3.28}$$

When the scaled matrix is sufficiently close to the origin a Padé approximation can be used to calculate φ_l. It is given by

$$\varphi_l(\mathbb{B}) = (D_d^l(\mathbb{B}))^{-1} N_d^l(\mathbb{B}) + \mathcal{O}(||\mathbb{B}||^{2d+1}) \tag{3.29}$$

with $\mathbb{B} \neq \mathbf{0}$ and where the polynomials N_d^l and D_d^l are given by

$$N_d^l(\mathbb{B}) = \frac{d!}{(2d+l)!} \sum_{i=0}^{d} \left[\sum_{j=0}^{i} \frac{(2d+l-j)!(-1)^j}{j!(d-j)!(l+i-j)!} \right] \mathbb{B}^i \tag{3.30}$$

$$D_d^l(\mathbb{B}) = \frac{d!}{(2d+l)!} \sum_{i=0}^{d} \frac{(2d+l-i)!(-1)^i}{i!(d-i)!} \mathbb{B}^i \tag{3.31}$$

To calculate an approximation for φ_1 we used a (7, 7) Padé approximant, i.e. $d = 7$.

3.4.4.2 Undoing the Scaling

To undo the scaling we utilise the fact that $\varphi_1(2\mathbb{B})$ can be calculated recursively from $\varphi_1(\mathbb{B})$. This recursion relation is ([29, 31])

$$\varphi_1(2\mathbb{B}) = \frac{1}{2}(e^{\mathbb{B}} + \mathbb{I})\varphi_1(\mathbb{B}) \tag{3.32}$$

where $\mathbb{I}$ is the identity matrix. Undoing the scaling is now straightforward. One only needs to apply this recurrence relation $k = max[0, p+1]$ times to $\varphi(\mathbb{B}_{sc})$ and one ends up with $\varphi(\mathbb{B})$.

3.4.5 Application

In order to use exponential integration we must construct our equation of motion in terms of linear terms and nonlinear terms. During this discussion we will omit the primes that denote dimensionless variables, however, the variables we discuss are assumed to be dimensionless. We do a linear expansion of the velocity around some point $\mathbf{r}_0$

$$\mathbf{u}(\mathbf{r}) = \mathbf{u}(\mathbf{r}_0) + \mathbb{A}(\mathbf{r}_0)(\mathbf{r} - \mathbf{r}_0) + \mathbf{N}(\mathbf{r}) \tag{3.33}$$

Introducing a new variable $\mathbf{q} = \mathbf{r} - \mathbf{r}_0 + \mathbb{A}(\mathbf{r}_0)^{-1}\mathbf{u}(\mathbf{r}_0)$ we arrive at the following equations of motion

$$\dot{\mathbf{q}} = \mathbf{v} \tag{3.34a}$$

$$\dot{\mathbf{v}} = \frac{1}{St}(\mathbb{A}\mathbf{q} - \mathbf{v}) + \frac{1}{St}\mathbf{N} \tag{3.34b}$$

Now we introduce $\mathbf{W} = [q_1, q_2, v_1, v_2]^T$ to write

$$\dot{\mathbf{W}} = \mathbb{C}\mathbf{W} + \mathbf{F}_N \tag{3.35}$$

with

$$\mathbb{C} = \begin{pmatrix} 0 & 0 & 1 & 0 \\ 0 & 0 & 0 & 1 \\ \frac{a_{11}}{St} & \frac{a_{12}}{St} & -\frac{1}{St} & 0 \\ \frac{a_{21}}{St} & -\frac{a_{11}}{St} & 0 & -\frac{1}{St} \end{pmatrix}, \qquad \mathbf{F}_N = \begin{pmatrix} 0 \\ 0 \\ \frac{1}{St}N_1 \\ \frac{1}{St}N_2 \end{pmatrix} \tag{3.36}$$

This results in a matrix differential equation with linear terms $\mathbb{C}$ and nonlinear terms $\mathbf{F}_N$. Note that $\mathbf{N} = \mathbf{u}(\mathbf{r}) - \mathbb{A}\mathbf{q}$ where $\mathbf{u}(\mathbf{r})$ is found by bicubic interpolation on the velocity field. We now have a form where we can use exponential integration. Appendix A contains information about some of the matrices derived from $\mathbb{C}$ required during exponential integration.

4

Results

4.1 Flow Statistics

This chapter is concerned with the statistics of the time-independent and the time dependent flow. The statistics of the flow snapshots are derived from Eq. (3.4b) and the time-dependent statistics are discussed in section 3.1.2.

4.1.1 Covariance of Flow Snapshots

We are interested in the statistics of the flow components and flow gradient components in two dimensions. The flow and flow gradients are derived from the stream function, whose mean is zero and covariance is given by Eq. (3.4b). From this one finds

$$\langle u_x(\mathbf{r})u_x(\mathbf{r}')\rangle = -\frac{l_\mathrm{f}^2 u_0^2}{2}\frac{(y-y')^2 - l_\mathrm{f}^2}{l_\mathrm{f}^4}e^{-||\mathbf{r}-\mathbf{r}'||^2/(2l_\mathrm{f}^2)} \tag{4.1}$$

$$\langle u_x(\mathbf{r})u_y(\mathbf{r}')\rangle = \frac{u_0^2}{2l_\mathrm{f}^2}(x-x')(y-y')e^{-||\mathbf{r}-\mathbf{r}'||^2/(2l_\mathrm{f}^2)} \tag{4.2}$$

$$\langle u_y(\mathbf{r})u_y(\mathbf{r}')\rangle = -\frac{l_\mathrm{f}^2 u_0^2}{2}\frac{(x-x')^2 - l_\mathrm{f}^2}{l_\mathrm{f}^4}e^{-||\mathbf{r}-\mathbf{r}'||^2/(2l_\mathrm{f}^2)} \tag{4.3}$$

where $||\cdot||$ denotes the Euclidean norm. Figure 4.1 shows how our numerical implementation of the velocity field (dots) compares to Eqs. (4.1) - (4.3) (solid lines). The statistics of the simulated flow velocities were calculated using 100 flow snapshots. The parameters used were $u_0 = 0.01$ and $l_\mathrm{f} = 0.1$. The flow snapshots were generated on the unit square (excluding the boundaries x = 1 and y = 1) with 200 grid points in each direction. We assume periodic boundary conditions such that $\mathbf{u}(x=1,y) = \mathbf{u}(x=0,y)$ and $\mathbf{u}(x,y=1) = \mathbf{u}(x,y=0)$. The agreement is good, with absolute error on the order of 10^{-5}. Although the figure only shows the line $\Delta y = -2\Delta x$, 15 other lines were simulated and the results were comparable to this case.

Similarly we can find the covariance between the different flow gradient components, as well as the covariance between the velocity and the gradients. For the flow

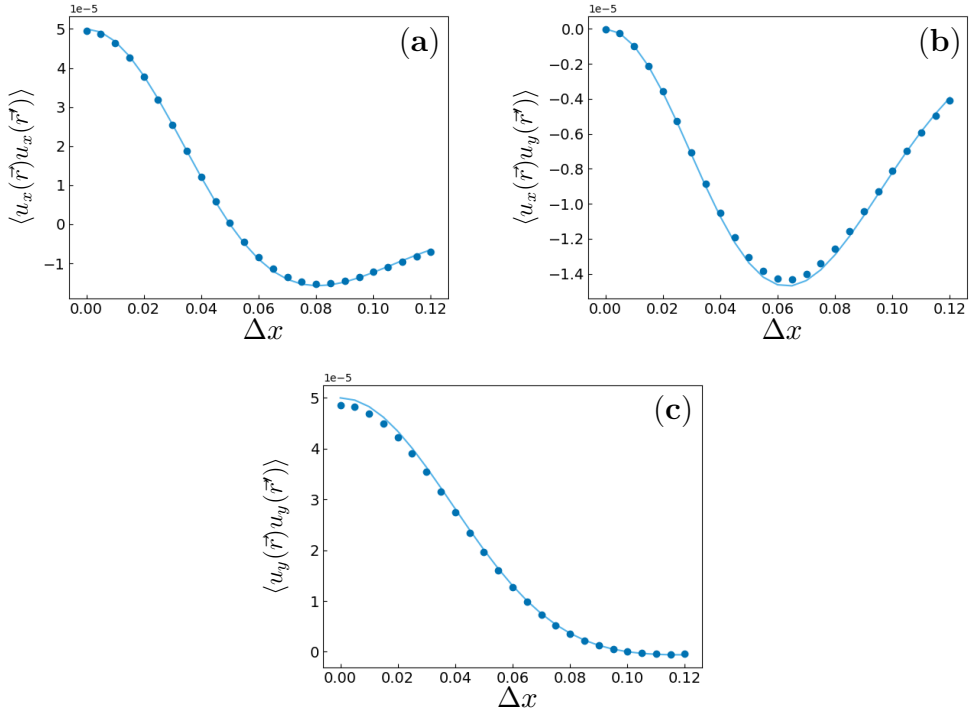

Figure 4.1: Covariance for velocity components. Panel (**a**) shows the covariance $\langle u_x(\vec{r})u_x(\vec{r}')\rangle$, panel (**b**) the covariance $\langle u_x(\vec{r})u_y(\vec{r}')\rangle$ and panel (**c**) the covariance $\langle u_y(\vec{r})u_y(\vec{r}')\rangle$. Data is obtained along the line $\Delta y = -2\Delta x$. The parameters used were $u_0 = 0.01$ and $l_\mathrm{f} = 0.1$.

gradient components one finds

$$\langle A_{11}(\mathbf{r})A_{11}(\mathbf{r}')\rangle = \frac{u_0^2}{2l_\mathrm{f}^6}((y-y')^2 - l_\mathrm{f}^2)e^{-||\mathbf{r}-\mathbf{r}'||^2/(2l_\mathrm{f}^2)} \tag{4.4}$$

$$\langle A_{11}(\mathbf{r})A_{12}(\mathbf{r}')\rangle = \frac{u_0^2}{2l_\mathrm{f}^6}(x-x')((y-y')^3 - 3l_\mathrm{f}^2(y-y'))e^{-||\mathbf{r}-\mathbf{r}'||^2/(2l_\mathrm{f}^2)} \tag{4.5}$$

$$\langle A_{11}(\mathbf{r})A_{21}(\mathbf{r}')\rangle = -\frac{u_0^2}{2l_\mathrm{f}^6}(y-y')((x-x')^3 - 3l_\mathrm{f}^2(x-x'))e^{-||\mathbf{r}-\mathbf{r}'||^2/(2l_\mathrm{f}^2)} \tag{4.6}$$

$$\langle A_{12}(\mathbf{r})A_{12}(\mathbf{r}')\rangle = \frac{u_0^2}{2l_\mathrm{f}^6}((y-y')^4 - 4l_\mathrm{f}^2(y-y')^2 + 3l_\mathrm{f}^4)e^{-||\mathbf{r}-\mathbf{r}'||^2/(2l_\mathrm{f}^2)} \tag{4.7}$$

$$\langle A_{21}(\mathbf{r})A_{21}(\mathbf{r}')\rangle = \frac{u_0^2}{2l_\mathrm{f}^6}((x-x')^4 - 4l_\mathrm{f}^2(x-x')^2 + 3l_\mathrm{f}^4)e^{-||\mathbf{r}-\mathbf{r}'||^2/(2l_\mathrm{f}^2)} \tag{4.8}$$

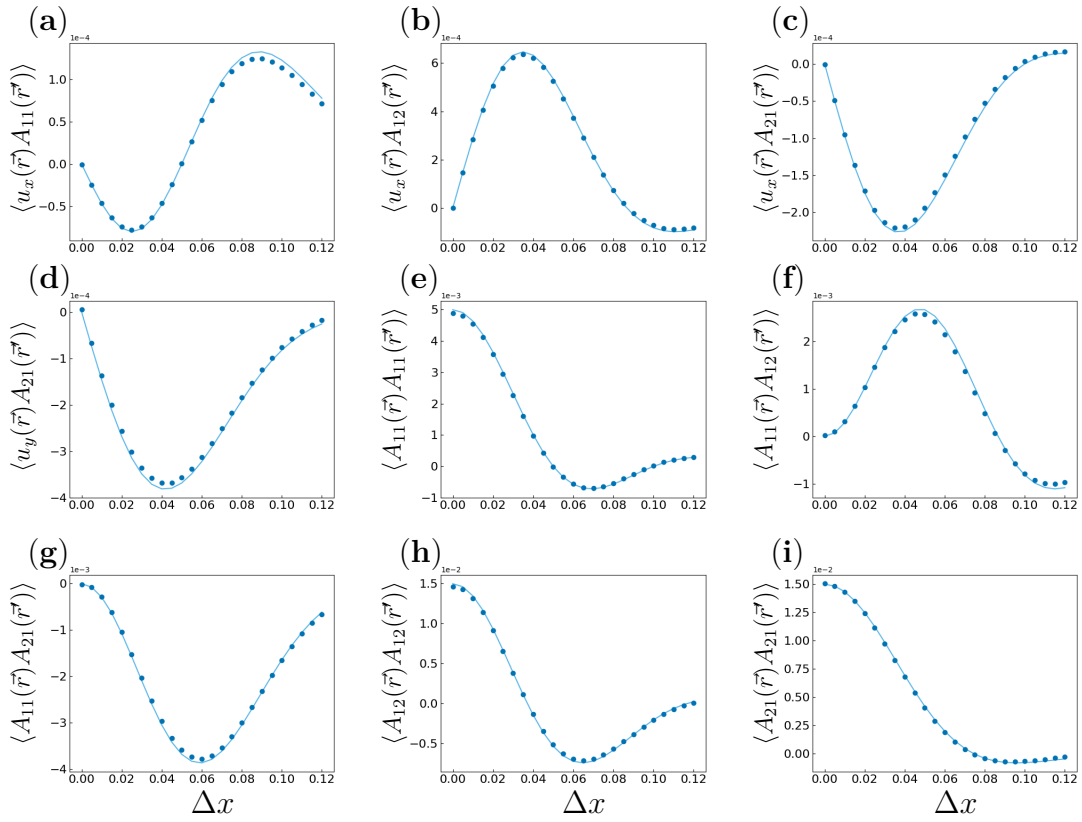

Figure 4.2: Covariance between velocity components and velocity gradient components, as well as between different velocity gradient components.

and for the covariance between velocities and gradients one finds

$$\langle u_x(\mathbf{r})A_{11}(\mathbf{r}')\rangle = \frac{u_0^2}{2l_\mathrm{f}^4}(x-x')((y-y')^2-l_\mathrm{f}^2)e^{-||\mathbf{r}-\mathbf{r}'||^2/(2l_\mathrm{f}^2)} \tag{4.9}$$

$$\langle u_x(\mathbf{r})A_{12}(\mathbf{r}')\rangle = \frac{u_0^2}{2l_\mathrm{f}^4}((y-y')^3-3l_\mathrm{f}^2(y-y'))e^{-||\mathbf{r}-\mathbf{r}'||^2/(2l_\mathrm{f}^2)} \tag{4.10}$$

$$\langle u_x(\mathbf{r})A_{21}(\mathbf{r}')\rangle = -\frac{u_0^2}{2l_\mathrm{f}^4}(y-y')((x-x')^2-l_\mathrm{f}^2)e^{-||\mathbf{r}-\mathbf{r}'||^2/(2l_\mathrm{f}^2)} \tag{4.11}$$

$$\langle u_y(\mathbf{r})A_{21}(\mathbf{r}')\rangle = \frac{u_0^2}{2l_\mathrm{f}^4}((x-x')^3-3l_\mathrm{f}^2(x-x'))e^{-||\mathbf{r}-\mathbf{r}'||^2/(2l_\mathrm{f}^2)} \tag{4.12}$$

Additionally $\langle u_y(\mathbf{r})A_{11}(\mathbf{r}')\rangle = \langle u_x(\mathbf{r})A_{21}(\mathbf{r}')\rangle$, $\langle u_y(\mathbf{r})A_{12}(\mathbf{r}')\rangle = -\langle u_x(\mathbf{r})A_{11}(\mathbf{r}')\rangle$ and $\langle A_{12}(\mathbf{r})A_{21}(\mathbf{r}')\rangle = -\langle A_{11}(\mathbf{r})A_{11}(\mathbf{r}')\rangle$. Keeping in mind that $A_{22} = -A_{11}$ we conclude that the covariances listed above characterise all the covariances for the two dimensional flow velocities and flow velocity gradients.

Figure 4.2 shows how the covariance of simulated velocities and velocity gradients (dots) compare to Eqs. (4.4) - (4.12) (solid lines). The parameters used were the same as in Figure 4.1. We observe good agreement between analytical and numerical results. Although only results corresponding to the line $\Delta y = -2\Delta x$ is shown, more trajectories were computed and all show similar results.

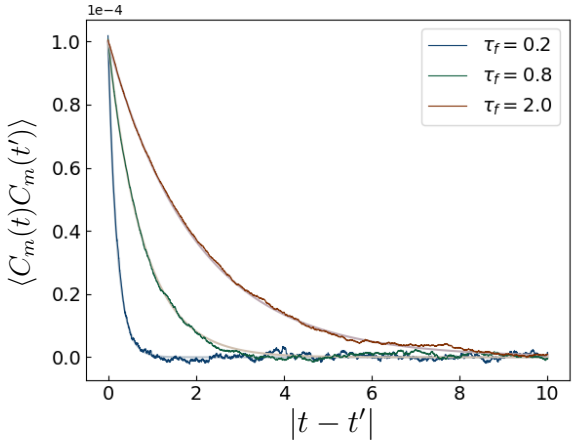

Figure 4.3: Covariance of the C coefficients as a function of time difference for different values of τ_{f}. The highlighted colours shows numerical results whereas the subdued colors show the corresponding analytical results.

4.1.2 Time Dependent Statistics

Two methods will be used to verify the time dependent statistics. Firstly the correlation of the C coefficients will be calculated and compared to Eq. (3.7). Secondly the probability density function for $u_x(\mathbf{r}, t)$ can be computed analytically for low values of M. One can thus sample the numerical result and compare the probability densities.
Figure 4.3 shows the covariance of the C coefficients. They are updated according to the scheme in section 3.1.2. The timestep is $dt = 0.001$, the number of iterations is $n_{iter} = 1000$, the number of coefficients is $M = 10000$ and the timescales of the flow correlations are $\tau_{\mathrm{f}} = 0.2$, $\tau_{\mathrm{f}} = 0.8$ and $\tau_{\mathrm{f}} = 2.0$. The highlighted colours show the numerical simulations and the corresponding subdued colours the analytical simulations. Good agreement is observed between the numerical simulation and the analytical result.
We now note that Eq. (3.6) expresses the time dependent velocity as a sum of products of two Gaussian variables. We have analytically calculated the probability density functions in the case $M = 1$, $M = 2$ and $M = 3$. Appendix B shows the derivation of these probability density functions, but they are given by

$$f_1(u_i) = \frac{1}{\pi\sigma_c\sigma_u} K_0\left(\frac{|u_i|}{\sigma_c\sigma_u}\right) \tag{4.13a}$$

$$f_2(u_i) = \frac{1}{2\sigma_u\sigma_c} e^{-\frac{|u_i|}{\sigma_u\sigma_c}} \tag{4.13b}$$

$$f_3(u_i) = \frac{|u_i|}{\pi\sigma_u^2\sigma_c^2} K_1\left(\frac{|u_i|}{\sigma_c\sigma_u}\right) \tag{4.13c}$$

Here K_0 and K_1 are modified Bessel functions of the second kind (See Appendix B for a detailed discussion), $\sigma_c = \frac{1}{\sqrt{M}}$ is the standard deviation of the random C coefficients and σ_u is the standard deviation of the flow velocity components (in two dimensions we have $\sigma_u = u_0/\sqrt{2}$).

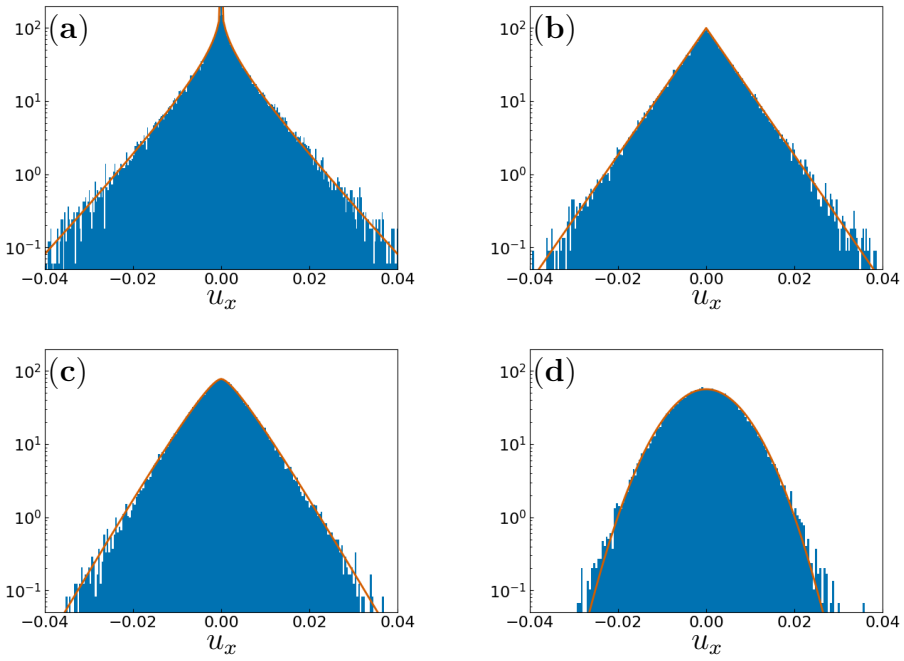

Figure 4.4: Comparison between the binned flow velocity component u_x and analytical probability density functions, Eq. (4.13). Panel (**a**) uses a superposition of $M = 1$ flow snapshots (Eq. (3.6)), panel (**b**) has $M = 2$, panel (**c**) has $M = 3$ and panel (**d**) has $M = 20$.

Figure 4.4 shows how the x component of the velocity from Eq. (3.6) compares to the analytical probability density function. The cases $M = 1$, $M = 2$ and $M = 3$ are shown in panels (**a**), (**b**) and (**c**), respectively, and in each case good agreement is found between the binned velocities and the analytical probability density functions. Finally, panel (**d**) shows the case $M = 20$. The analytical distribution is approximated as the normal distribution, $f(u_i) = \frac{1}{\sqrt{2\pi\sigma_u^2}}\exp(-\frac{u_i^2}{2\sigma_u^2})$, and we see a good fit, indicating that we are in the range where the central limit theorem is valid. We note the much heavier tails in the distributions where $M \in \{1, 2, 3\}$.

Get second opinion on this paragraph

4.2 Accuracy of the Interpolation Algorithm

To estimate the error of the interpolation algorithm we introduce a test function on the unit square:

$$f(x, y) = \sin(2\pi x)(\cos(4\pi y) - \pi) \tag{4.14}$$

A contour plot of this function can be seen in Figure 4.5. A notable property of this function is its periodicity; in both x- and y-direction the function's period is a whole number multiple of the simulation box length (which is one in this case). The function is stored on a the same grid as the flow snapshots. This allows us to check the performance of the interpolation algorithm and also account for the periodic boundary conditions.

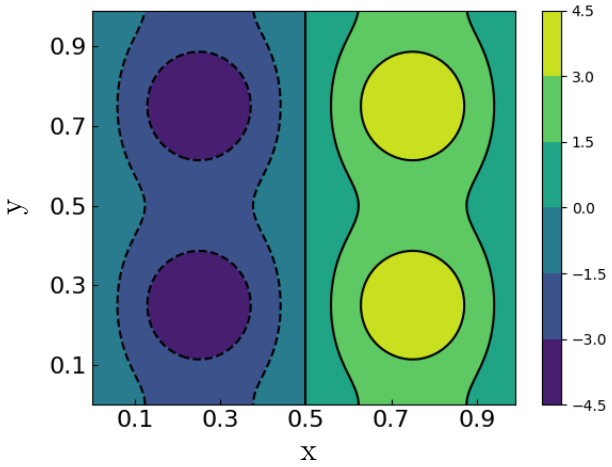

Figure 4.5: A contour plot of the test function (4.14) on the unit square.

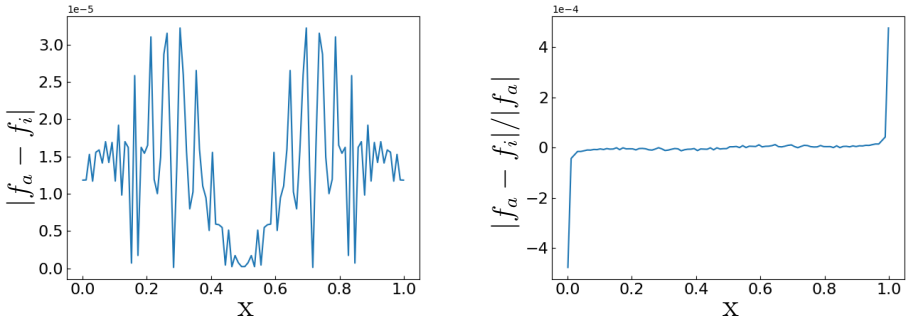

Figure 4.6: The absolute and relative interpolation errors along the trajectory $y = 0.2 + 0.6x$ for the test function (4.14). In the y-label $f_a = f_a(x, y)$ denotes the analytical function value at the point (x, y) whereas $f_i = f_i(x, y)$ denotes the interpolated value at that point.

The absolute and relative interpolation errors along the line $y = 0.2 + 0.6x$ are shown in figure 4.6. The absolute error shows a periodic trend, with an amplitude of order of magnitude 10^{-5}. The magnitude of the relative error peaks around 10^{-4}, taking that value at the boundaries. We note that the function values are zero at the boundaries, so we expect divergence in the relative error close to the boundaries, which is exactly what is observed. When it doesn't diverge, the relative error has magnitude at least an order of magnitude lower than those peaks, i.e. 10^{-5}, meaning the agreement between interpolated values and analytical values is good.

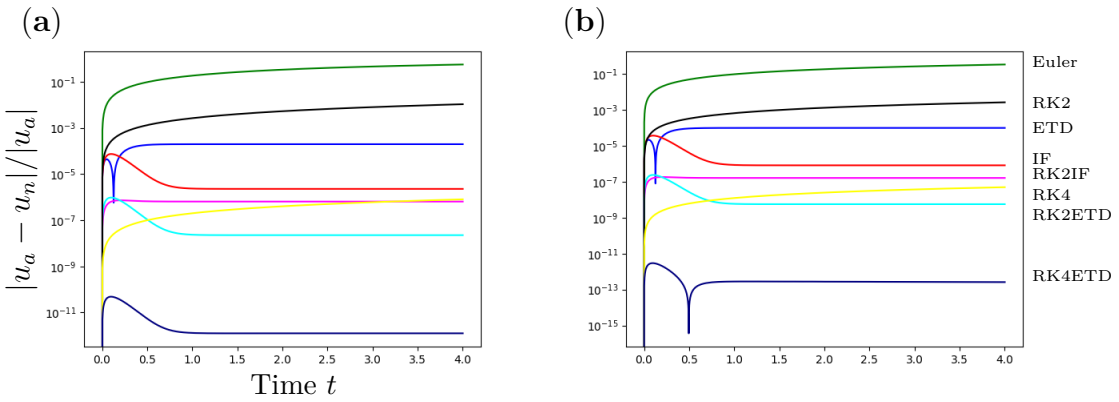

Figure 4.7: The relative error for various integrating methods as a function of time when solving the initial value problem (4.15). On the y-axis u_a denotes the analytical solution of the velocity and u_n the numerical solution. The timestep used was (**a**): $h = 1/2^8$ and (**b**): $h = 1/2^9$.

4.3 Particle Dynamics

4.3.1 Integration in One and Two Dimensions

We now want to test the performance of the exponential integration scheme (3.26). To that end we consider the initial value problem

$$\frac{du(t)}{dt} = -10u(t) + \sin(t)u(t)^2 \tag{4.15a}$$
$$u(0) = 1 \tag{4.15b}$$

in one dimension. The solution to this initial value problem is given by (Found using Mathematica)

$$u(t) = \frac{101}{100e^{10t} + 10\sin(t) + \cos(t)}. \tag{4.16}$$

This allows us to compare the numerical result of various integration methods to the exact solution. The methods we will compare are integrating factor (IF) methods of first and second order (based on Euler and second order Runge-Kutta), exponential time differencing (ETD) methods of order 1, 2, and 4 where the second and fourth order methods are Runge-Kutta methods, and finally the classical (without exponential integration) forward Euler and Runge-Kutta (RK) methods of order 2 and 4. These methods are described in Appendix C.
The performance of the various methods is shown in Figure 4.7 for two different timesteps, (**a**): $h = 1/2^8$ and (**b**): $h = 1/2^9$. In both cases the forward Euler method performs the worst, followed by the classical second order Runge-Kutta method. We also observe that the peak error for the first order IF and ETD methods have similar magnitude, but overall the IF method has lower errors, which for large values of t has similar error values to RK4 and the RK2IF method. It should be noted that the peak errors of those methods are significantly lower. The peak errors of RK2IF and RK2ETD have the same magnitude. Finally, the method that performs the best is the RK4ETD method, with initial error values roughly 2 orders

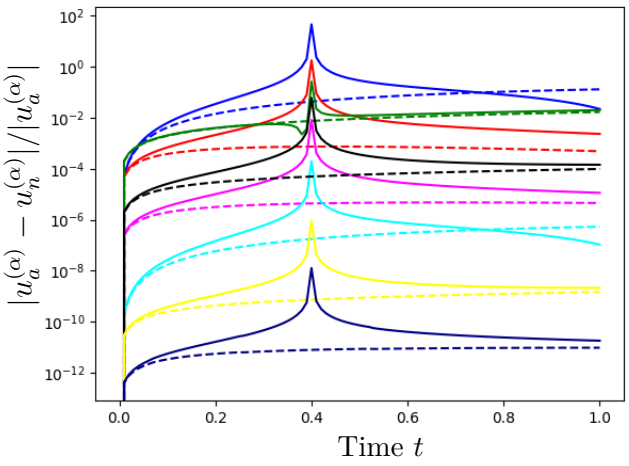

Figure 4.8: The relative errors for the same numerical schemes as in Figure 4.7 as functions of time. Dashed lines show the relative error in the x-component and solid line the relative errors in the y-component. In the y-label the superscript (α) is used to denote that this error is componentwise. The timestep is taken as $h = 0.01$.

of magnitude lower than other methods and persistent error values (i.e. for large t) close to 4 orders of magnitude lower.

Next we consider a similar problem in two dimensions. The problem we want to solve is

$$\begin{aligned} \tfrac{d}{dt}\mathbf{z} &= \mathbb{A}\mathbf{z} + \sin(t)\mathbf{1} && \text{(4.17a)} \\ \mathbf{z}(0) &= (1,1)^T && \text{(4.17b)} \end{aligned}$$

with $\mathbb{A} = \begin{bmatrix} 2 & 1 \\ -1 & -2 \end{bmatrix}$. Writing $\mathbf{z} = (x, y)^T$, this initial value problem has the solution

$$\begin{aligned} x(t) &= \frac{1}{8}e^{-\sqrt{3}t}\left(5 - 5\sqrt{3} + 5e^{2\sqrt{3}t} + 5\sqrt{3}e^{2\sqrt{3}t}\right) \\ &\quad + \frac{1}{8}e^{-\sqrt{3}t}\left(-2e^{\sqrt{3}t}\cos(t) - 6e^{\sqrt{3}t}\sin(t)\right) && \text{(4.18)} \\ y(t) &= -\frac{1}{8}e^{-\sqrt{3}t}\left(-5 - 5\sqrt{3} - 5e^{2\sqrt{3}t} + 5\sqrt{3}e^{2\sqrt{3}t}\right) \\ &\quad - \frac{1}{8}e^{-\sqrt{3}t}\left(2e^{\sqrt{3}t}\cos(t) - 6e^{\sqrt{3}t}\sin(t)\right) && \text{(4.19)} \end{aligned}$$

Looking at Figure 4.8 we notice that once again the RK4ETD method outperforms all other methods by orders of magnitude. This time the worst performing method is surprisingly ETD, with Euler and IF the second worst. The second best method is RK4 and the third best is RK2ETD. The timestep during these simulations was $h = 0.01$.

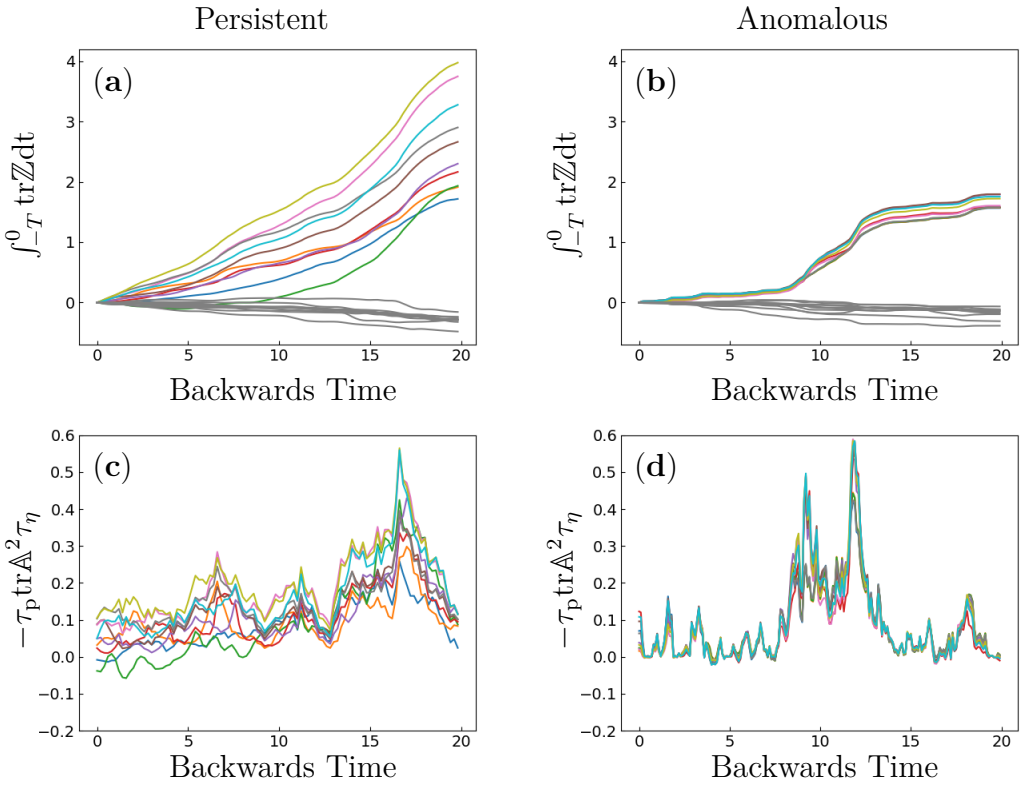

Figure 4.9: Panels (**a**) and (**b**) show the integral $\int_{-T}^{0} \mathrm{tr}\mathbb{Z}\mathrm{dt}$ as a function of time when the total integration time is $T = 20\tau_\eta$. In color are the ten histories which result in the largest value of the integral and in gray we plot random histories not among the ten largest. Panel (**a**) corresponds to the persistent case and panel (**b**) to the anomalous case. Panels (**c**) and (**d**) show the instantaneous values of $-\tau_p \mathrm{tr}\mathbb{A}^2\tau_\eta$ for the 10 colored trajectories in panels (**a**) and (**b**) as a function of backwards time. Panel (**c**) corresponds to the persistent case and panel (**d**) to the anomalous case.

4.4 Void Formation

The integral in Eq. (2.24) is evaluated numerically using two models. First we consider the persistent limit, with Ku = 10 and St = 0.02. Secondly we consider the anomalous limit, where Ku = 1 and St = 0.02. In both cases the time dependent flow is written as a superposition of $M = 3$ flow snapshots.
Panels (**a**) and (**b**) in figure 4.9 show the value of the integral at every point in time for the ten trajectories resulting in the largest integrals when the total backwards integration time is chosen as $T = 20\tau_\eta$ (shown in color) as well as for ten random trajectories not part of the ten largest (shown in gray). Panel (**a**) corresponds to the persistent case and panel (**b**) to the anomalous case. There are two main differences that we observe. Firstly, the shape of the integral in the persistent case is smoother, i.e. it has more jumps, but each jump is small. Secondly the magnitude of the integral in the persistent case is much larger than in the anomalous case. Since the integral is a measure of how sparsely populated the surrounding area is, it goes to show that void formation is much easier in the persistent case compared to the anomalous case.

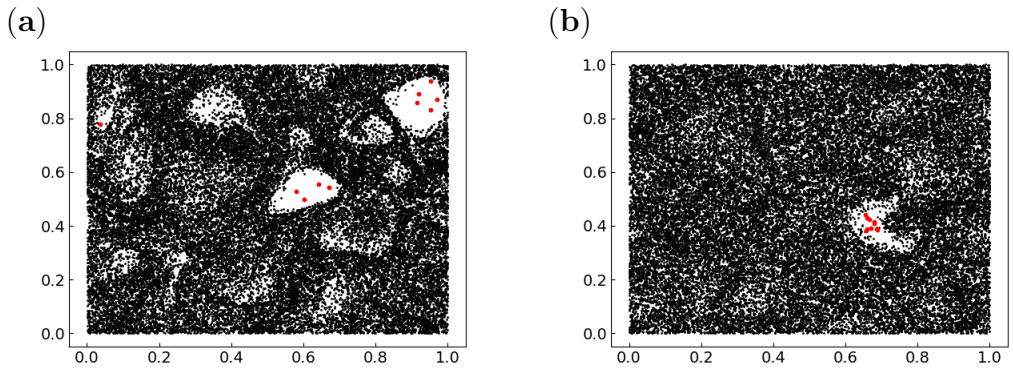

Figure 4.10: Snapshot of particle positions at $t = 0$. Particles leading to a large value of the integral are shown in red, others in black. Panel (**a**) shows the persistent limit, panel (**b**) the anomalous limit.

If we now look at panels (**c**) and (**d**) we see the instantaneous values of $-\tau_{\mathrm{p}}\mathrm{tr}\mathbb{A}^2\tau_\eta$ for the 10 colored trajectories in panels (**a**) and (**b**) as a function of the backwards time. Panel (**c**) corresponds to the persistent case and panel (**d**) to the anomalous case. Again we note the smaller magnitude in the anomalous case. In the persistent case the vortex appears to live longer, with slightly lower magnitude, whereas in the anomalous case the vortex lives shorter with a slightly larger magnitude. This is consistent with our hypothesis from section 2.5 where we surmised that void formation must either be due to a long standing vortex of moderate strength or a short lived vortex of great strength.

A snapshot of the particle positions, at the final time, $t = 0$, can be seen in Figure 4.10. Particles with histories that lead to a large value of the integral are shown in red, other in black. Panel (**a**) shows the persistent limit, panel (**b**) the anomalous limit.

The method we used to sample the history is to save the state of the system periodically during forwards integration and then evaluating the history integral using those saved states. Another method has been proposed [14], which involves integrating the dynamics of tracer particles backwards in time, starting from the final state of the forward integration (t = 0). To compare the two methods we have utilised both methods on the anomalous system from before.

Figure 4.11 compares the two methods. Panels (**a**) and (**c**) correspond to (**b**) and (**d**) in Figure 4.9 and as such show the integral $\int_{-T}^{0}\mathrm{tr}\mathbb{Z}\mathrm{dt}$ and $-\tau_{\mathrm{p}}\mathrm{tr}\mathbb{A}^2\tau_\eta$ in the anomalous case. In this case the history is sampled during the forward dynamics, and is then used to evaluate the integral. Panels (**b**) and (**d**) show the integral $\int_{-T}^{0}\mathrm{tr}\mathbb{Z}\mathrm{dt}$ and $-\tau_{\mathrm{p}}\mathrm{tr}\mathbb{A}^2\tau_\eta$ for same system, now evolved by integrating the dynamics of tracer particles backwards in time, starting from the final state of the forwards dynamics. A noticable difference is observed, the trajectories in panel (**b**) are more spread out than in panel (**a**) and the form of the instantaneous $-\tau_{\mathrm{p}}\mathrm{tr}\mathbb{A}^2\tau_\eta$ is different as well. However, the differences don't seem to significantly alter the results, the backwards integration method would still in most cases identify the same voids as sampling the forward dynamics. Only the resulting shape of the observed void might be distorted somewhat.

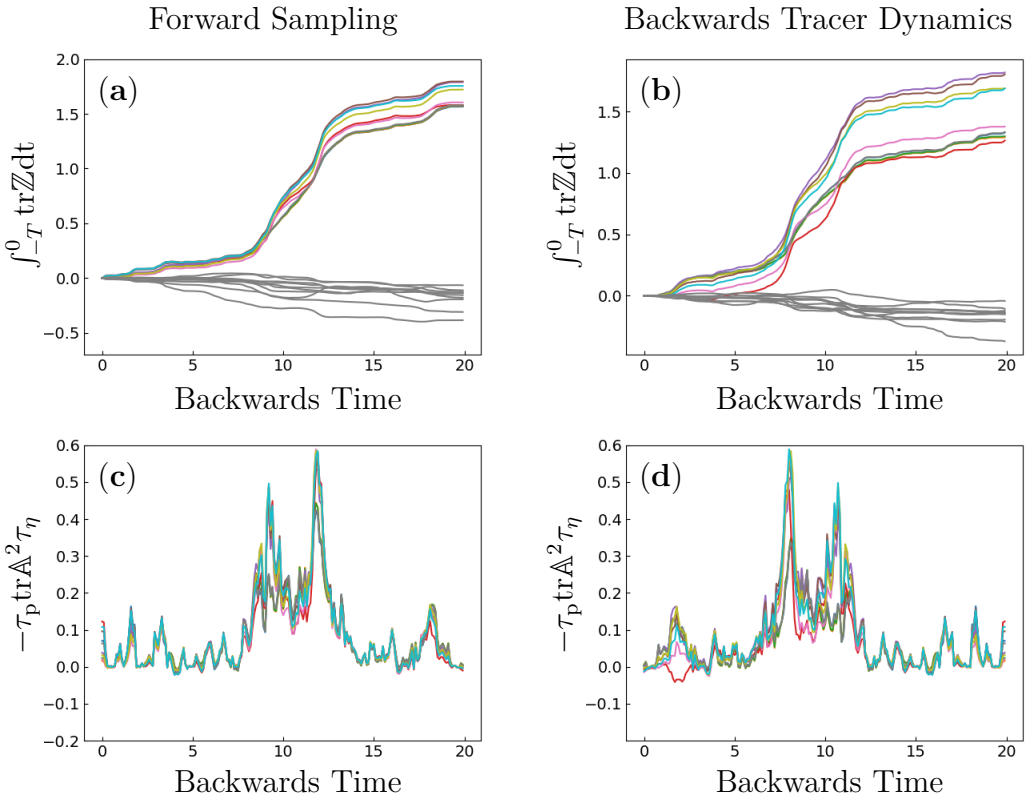

Figure 4.11: Panels (**a**) and (**c**) show the integral $\int_{-T}^{0} \mathrm{tr}\mathbb{Z}\mathrm{dt}$ and $-\tau_p \mathrm{tr}\mathbb{A}^2\tau_\eta$ in the anomalous case, and are the same as panels (**b**) and (**d**) in Figure 4.9. The history is sampled during the forward integration and uses the inertial dynamics. Panels (**b**) and (**d**) show the same, however the dynamics of tracer particles are integrated backwards in time, starting from the final state of the forward dynamics.

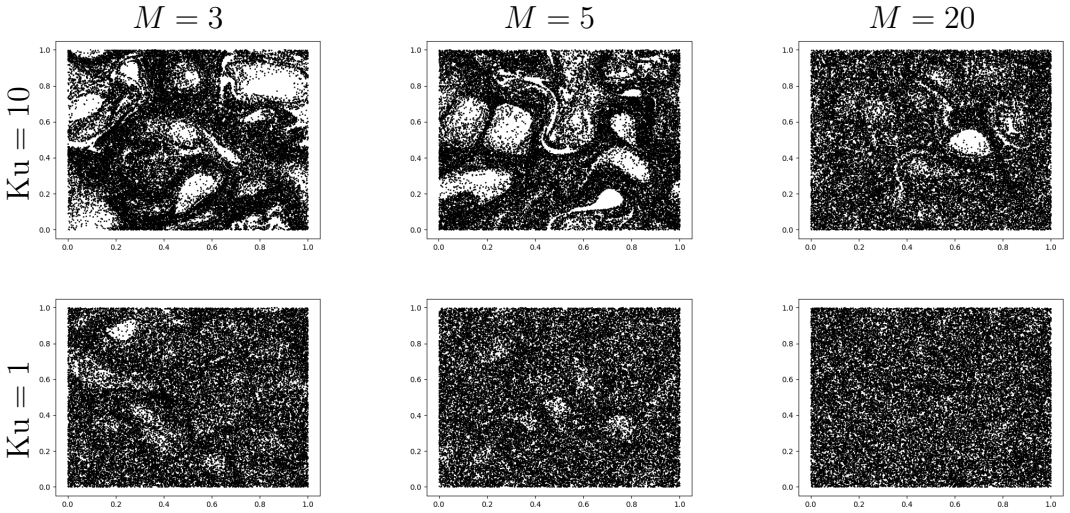

Figure 4.12: Void formation in the persistent (Ku = 10) and anomalous (Ku = 1) limit for two non-Gaussian flow models and a close to Gaussian model ($M = 20$).

Finally we want to find out how important the heavy tails of the non-Gaussian distribution are for void formation. Figure 4.12 shows the void formation for three different flow models in the persistent and anomalous limits. In each case 100 images were generated and an image was chosen amongst those which had the most extreme void formation. Looking first at the persistent case (Ku = 10), it is clear that the heavier tails in the non-Gaussian flow models ($M = 3$ and $M = 5$ in Eq. (3.6)) increase void formation compared to the close to Gaussian ($M = 20$) flow model. Not much difference is observed between the $M = 3$ model and the $M = 5$ model, though it should be noted that the most extreme cases observed for $M = 3$ had more voids than the $M = 5$ model, see figure 4.13. Looking now at the anomalous (Ku = 1) case, the void formation should be due to rare events, and as such should be nowhere near as prevalent. Indeed, only in the $M = 3$ model do we find clear signs of void formation. In the $M = 5$ case thinning of the particle distribution is observed but the vortices don't seem to be strong enough and long-lived enough to actually expel all particles. As such minimal vortex formation is observed. Finally, for the close to Gaussian model, no void formation is observed. Intuitively, this makes sense, since the heavier tales make finding extreme values more likely, which in turn makes strong vortex formation more likely. Though these results are purely observational, they seem to suggest that the importance of the non-Gaussian tails is significant.

4.5 Preferential Sampling

In section 2.3.1 we found that under a perturbative expansion, one expects a relation $\mathrm{tr}\langle \mathbb{A}^2 \rangle \tau_\eta^2 \sim \mathrm{St}$ to hold for small values of St.
Figure 4.14 shows the average $\mathrm{tr}\mathbb{A}^2\tau_\eta^2$ along particle paths as a function of the Stokes number. Panel (**a**) shows numerical results based on the model (3.6) and the dynamics (2.12). The black markers correspond to a Gaussian flow model, i.e.

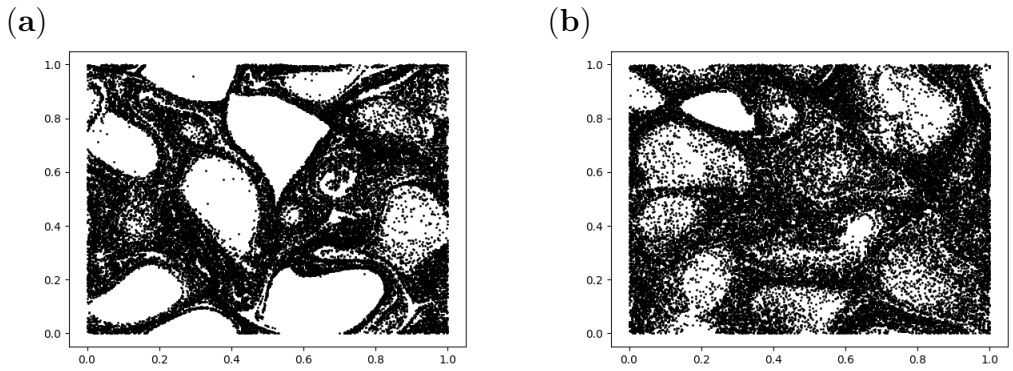

Figure 4.13: Extreme void formation for the flow model described by Eq. (3.6) for (**a**) $M = 3$ and (**b**) $M = 5$. Figures are chosen amongst 100 images in the persistent limit.

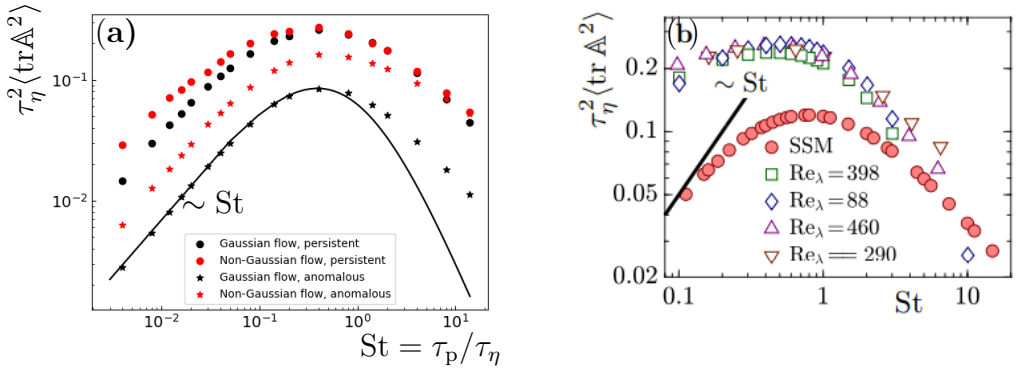

Figure 4.14: Average $\mathrm{tr}\mathbb{A}^2\tau_\eta^2$ along partice paths as a function of the Stokes number, St. Panel (**a**) shows numerical results from the model (3.6). Panel (**b**) is taken from Reference [11] with permission from authors and shows the average for a Gaussian statistical model (red dots) as well as multiple DNS simulations (unfilled shapes). It should be noted that the results in panel (**b**) are obtained for three dimensional flow.

we take $M = 20$ in the model (3.6). Similarly, the non-Gaussian model has $M = 3$ and is indicated by red markers. Now, the dots are measured in a persistent flow field, which simply means that $\tau_f = 1$, or equivalently, $\mathrm{Ku} = 10$. This long flow correlation time results in long lived flow structures and as such a persistent flow field. In a similar fashion, the anomalous flow field, with measurements marked by stars, corresponds to $\tau_f = 0.1$, or equivalently $\mathrm{Ku} = 1$. Now, the solid line is based on a small Ku derivation from [5],

for the Gaussian model?

$$\tau_\eta^2 \langle \mathrm{tr}\mathbb{A}^2 \rangle = \frac{3}{2} \frac{\mathrm{Ku}^2 \mathrm{St}}{(1+\mathrm{St})^2(1+2\mathrm{St})} \tag{4.20}$$

Note that at $\mathrm{Ku} = 1$ this expansion is not fully valid, but by changing the prefactor from $3/2 \to 3/4$ we get the fit seen in Figure (4.14). The most notable observation is the $\sim \mathrm{St}$ scaling at low Stokes numbers. At low Kubo numbers the same scaling seems to hold for the non-Gaussian model. However, at larger Kubo numbers (i.e. the persistent case) the non-Gaussian model seems to have a slightly smaller scaling exponent than the Gaussian model. This scaling relation seems closer to the DNS results observed in panel (**b**). The figure in panel (**b**) is taken from [11] with permission from the authors. In red are numerical results from a Gaussian statistical model, which show the same $\sim \mathrm{St}$ trend as we observed from the Gaussian model in panel (**a**). The unfilled shapes show DNS results from various simulations. All of them show a different scaling exponent than the Gaussian simulation does at low values of St. The results are obtained in three dimensions and for $\mathrm{Ku} = 10$.
Our hypothesis as to why the non-Gaussian simulation in the persistent case is closer to the DNS simulations is that the heavier tails of the non-Gaussian distribution lead to increased sampling of the straining regions of the flow compared to a Gaussian distribution (i.e. it accentuates the preferential sampling effect described by Maxey's centrifuge mechanism). This would lead to particles on average having larger values of $\mathrm{tr}\mathbb{A}^2$, which ends up giving results closer to those observed during DNS. As for why this is not observed in the anomalous flow, we suspect it may be because at such low Ku values, the particles generally don't have enough time to gather in straining regions before flow correlations are completely gone.

5

Discussion and Conclusion

This project aimed to understand the importance of statistical distributions with heavy tails when modelling turbulence using such models. A statistical description of turbulence was obtained by generating flow snapshots using a sum of Fourier coefficients. These flow snapshots had a Gaussian spatial covariance, and when a superposition of such flow snapshots was taken, with each snapshot weighted by a zero mean Gaussian random coefficient, we could control the distribution of the resulting velocity field to some degree. A superposition of fewer snapshots resulted in heavier tails, whereas with very many snapshots the distribution of the time dependent flow approached the normal distribution.

We were interested in the properties of particles in such a flow. Small, heavy and spherical particles can detach from the flow, and this leads to phenomena such as preferential sampling, fractal clustering and void formation. Comparing measurable quantities related to these phenomena, we can compare the properties of the particles in the non-Gaussian flow to other models, especially the Gaussian flow model. These comparisons are observed in figures 4.9 - 4.14.
Figures 4.9 - 4.13 show results on void formation. Figure 4.9 demonstrates the two types of events that can cause void formation, namely persistent vortices and anomalously strong vortices. Figure 4.11 compares methods of evaluating the history integral, showing that unless great accuracy is required, both methods should detect void formation quite well. Although the backwards integration is a bit less accurate, it has the benefit that it can have arbitrary starting conditions, i.e. we don't have to rely on looking only into histories of particles which happen to end up in a void. Finally figure 4.12 highlights the importance of the non-Gaussian model. For the Gaussian model, minimal void formation is observed in the persistent case and none in the anomalous case. However, for the non-Gaussian model, void formation is observed in both cases, and to quite a substantial degree in the persistent case. Moving forward, a quantitative analysis of the impact of the non-Gaussian model could further strengthen the findings presented here.
Figure 4.14 shows the degree of preferential sampling of $\mathrm{tr}\mathbb{A}^2$. It measures the average $\mathrm{tr}\mathbb{A}^2\tau_\eta^2$ along particle paths as a function of the Stokes number. At large Kubo numbers we see a slight difference between the scaling exponentials of the Gaussian model and the non-Gaussian model, whereas that difference is practically non-existent for the lower Kubo number. We hoped that the heavy tails of the non-Gaussian distribution could shed some light on the difference between the DNS results and statistical results observed, and the difference at $\mathrm{Ku} = 10$ is promising but more simulations should be done for a more conclusive result. For one, we

should verify that eq. (4.20) is valid for the Gaussian model at lower Ku, e.g. at Ku = 0.2, where we expect a good match for the range of Stokes numbers we consider. Additionally, we should see whether the difference between the models grows larger at larger Kubo numbers, and possibly try to compare it to DNS results. We should also perform simulations in three-dimensions so that we can directly make comparisons between our models and DNS results. Finally, we should verify the results using a better integration method, one that correctly integrates the dynamics of anomalously large fluctuations in the non-Gaussian model. With such a solver, and available data from DNS, one could integrate the dynamics to also verify that the small St DNS results in figure 4.14 (**b**) are correct.
Unfortunately, due to time constraints, we didn't manage to obtain results regarding fractal clustering. Additionally, getting the fourth order exponential integrator to work for the time dependent flow field has proven a bigger obstacle than we originally imagined, but we would like to bolster our findings on preferential sampling by doing the same analysis with an integrator specifically designed for stiff differential equations. That will, however, have to wait, as we still haven't managed to fix the problem with the integrator.

Overall, we found that the impact of the heavy tails in the non-Gaussian model was mostly consistent with our expectations, though it was a bit less than expected for preferential sampling and a bit greater than expected for void formation. Future research could focus on testing different types of probability distributions. Perhaps a way to model multiple scales of turbulence could be found, e.g. by shifting the distribution or by using a biased distribution. Additionally, so far we have only considered non-interacting particles, so a logical next step would be to include particle collisions in the model.

Bibliography

[1] Jeffrey S Guasto, Roberto Rusconi, and Roman Stocker. "Fluid mechanics of planktonic microorganisms". In: *Annual Review of Fluid Mechanics* 44 (2012), pp. 373–400.

[2] Volker Hessel, Holger Löwe, and Friedhelm Schönfeld. "Micromixers—a review on passive and active mixing principles". In: *Chemical engineering science* 60.8-9 (2005), pp. 2479–2501.

[3] Katarzyna Karpińska et al. "Turbulence-induced cloud voids: observation and interpretation". In: *Atmospheric Chemistry and Physics* 19.7 (2019), pp. 4991–5003.

[4] Martin R Maxey. "The gravitational settling of aerosol particles in homogeneous turbulence and random flow fields". In: *Journal of fluid mechanics* 174 (1987), pp. 441–465.

[5] K Gustavsson and B Mehlig. "Statistical models for spatial patterns of heavy particles in turbulence". In: *Advances in Physics* 65.1 (2016), pp. 1–57.

[6] Stephen B Pope. "Turbulent flows". In: *Measurement Science and Technology* 12.11 (2001), pp. 2020–2021.

[7] Lev Davidovich Landau and Evgenii Mikhailovich Lifshitz. *Fluid mechanics: Landau And Lifshitz: course of theoretical physics, Volume 6*. Vol. 6. Elsevier, 2013.

[8] Uriel Frisch. *Turbulence: the legacy of AN Kolmogorov*. Cambridge university press, 1995.

[9] Josiah Willard Gibbs and Edwin Bidwell Wilson. *Vector analysis: A text-book for the use of students of mathematics and physics, founded upon the lectures of j. willard gibbs*. Yale University Press, 1901.

[10] Joseph C Kolecki. *An introduction to tensors for students of physics and engineering*. Tech. rep. 2002.

[11] J Bec, K Gustavsson, and B Mehlig. "Statistical models for the dynamics of heavy particles in turbulence". In: *Annual Review of Fluid Mechanics* 56 (2024), pp. 189–213.

[12] J Meibohm et al. "Caustic formation in a non-Gaussian model for turbulent aerosols". In: *Physical Review Fluids* 9.2 (2024), p. 024302.

[13] Martin R Maxey and James J Riley. "Equation of motion for a small rigid sphere in a nonuniform flow". In: *The Physics of Fluids* 26.4 (1983), pp. 883–889.

[14] Gregory Falkovich and Alain Pumir. "Intermittent distribution of heavy particles in a turbulent flow". In: *Physics of Fluids* 16.7 (2004), pp. L47–L50.

[15] Jeremie Bec. “Fractal clustering of inertial particles in random flows”. In: *Physics of fluids* 15.11 (2003), pp. L81–L84.
[16] James L Kaplan and James A Yorke. “Chaotic behavior of multidimensional difference equations”. In: *Functional Differential Equations and Approximation of Fixed Points: Proceedings, Bonn, July 1978*. Springer, 2006, pp. 204–227.
[17] Edward Ott. *Chaos in dynamical systems*. Cambridge university press, 2002.
[18] John C Sommerer and Edward Ott. “Particles floating on a moving fluid: A dynamically comprehensible physical fractal”. In: *Science* 259.5093 (1993), pp. 335–339.
[19] François Ledrappier and L-S Young. “Dimension formula for random transformations”. In: (1988).
[20] Federico Toschi and Eberhard Bodenschatz. “Lagrangian properties of particles in turbulence”. In: *Annual review of fluid mechanics* 41 (2009), pp. 375–404.
[21] Eric Rosenberg. *Fractal dimensions of networks*. Vol. 1. Springer, 2020.
[22] Raymond A Shaw et al. “Preferential concentration of cloud droplets by turbulence: Effects on the early evolution of cumulus cloud droplet spectra”. In: *Journal of the atmospheric sciences* 55.11 (1998), pp. 1965–1976.
[23] A Pumir and J Sierra-Ausin. “Discussion on Void Formation in Clouds”. Private Discussion, 2024.
[24] H Sigurgeirsson and Andrew M Stuart. “A model for preferential concentration”. In: *Physics of Fluids* 14.12 (2002), pp. 4352–4361.
[25] Saul A Teukolsky et al. “Numerical recipes in C”. In: *SMR* 693.1 (1992), pp. 59–70.
[26] Paul Matthews. *Exponential integrators for stiff systems*. `https://indico.ictp.it/event/a08165/session/7/contribution/4/material/0/0.pdf`. June 2009.
[27] Steven M Cox and Paul C Matthews. “Exponential time differencing for stiff systems”. In: *Journal of Computational Physics* 176.2 (2002), pp. 430–455.
[28] Aly-Khan Kassam and Lloyd N Trefethen. “Fourth-order time-stepping for stiff PDEs”. In: *SIAM Journal on Scientific Computing* 26.4 (2005), pp. 1214–1233.
[29] Håvard Berland, Bård Skaflestad, and Will M Wright. “EXPINT—A MATLAB package for exponential integrators”. In: *ACM Transactions on Mathematical Software (TOMS)* 33.1 (2007), 4–es.
[30] Marlis Hochbruck and Alexander Ostermann. “Exponential integrators”. In: *Acta Numerica* 19 (2010), pp. 209–286.
[31] Marlis Hochbruck, Christian Lubich, and Hubert Selhofer. “Exponential integrators for large systems of differential equations”. In: *SIAM Journal on Scientific Computing* 19.5 (1998), pp. 1552–1574.
[32] Larisa Beilina, Evgenii Karchevskii, and Mikhail Karchevskii. *Numerical linear algebra: Theory and applications*. Springer, 2017.
[33] Milton Abramowitz and Irene A Stegun. *Handbook of mathematical functions with formulas, graphs, and mathematical tables*. Vol. 55. US Government printing office, 1948.

[34] Francesco Mainardi. *Fractional calculus and waves in linear viscoelasticity: an introduction to mathematical models*. World Scientific, 2022.

[35] Timothy Sauer. *Numerical analysis*. Addison-Wesley Publishing Company, 2011.

A

Matrix Calculations

Here we present some of the matrices derived from $\mathbf{C}$ defined in Eq. (3.36). The software Mathematica was used for most derivations. For simplicity of writing we set

$$\mathbf{C} = \begin{pmatrix} 0 & 0 & 1 & 0 \\ 0 & 0 & 0 & 1 \\ \frac{a}{s} & \frac{b}{s} & -\frac{1}{s} & 0 \\ \frac{c}{s} & -\frac{a}{s} & 0 & -\frac{1}{s} \end{pmatrix} \tag{A.1}$$

Then

$$\mathbf{C}^2 = \begin{pmatrix} \frac{a}{s} & \frac{b}{s} & -\frac{1}{s} & 0 \\ \frac{c}{s} & -\frac{a}{s} & 0 & -\frac{1}{s} \\ -\frac{a}{s^2} & -\frac{b}{s^2} & \frac{1}{s^2}+\frac{a}{s} & \frac{b}{s} \\ -\frac{c}{s^2} & \frac{a}{s^2} & \frac{c}{s} & \frac{1}{s^2}-\frac{a}{s} \end{pmatrix} \tag{A.2}$$

Let us define $\varsigma \stackrel{\text{def}}{=} a^2 + bc$. Then

$$\mathbf{C}^{-1} = \begin{pmatrix} \frac{a}{\varsigma} & \frac{b}{\varsigma} & \frac{as}{\varsigma} & \frac{bs}{\varsigma} \\ \frac{c}{\varsigma} & \frac{-a}{\varsigma} & \frac{cs}{\varsigma} & -\frac{as}{\varsigma} \\ 1 & 0 & 0 & 0 \\ 0 & 1 & 0 & 0 \end{pmatrix} \tag{A.3}$$

$$\mathrm{C}^{-2} = \begin{pmatrix} \frac{1+as}{\varsigma} & \frac{bs}{\varsigma} & \frac{s}{\varsigma} & 0 \\ \frac{cs}{\varsigma} & \frac{1-as}{\varsigma} & 0 & \frac{s}{\varsigma} \\ \frac{a}{\varsigma} & \frac{b}{\varsigma} & \frac{as}{\varsigma} & \frac{bs}{\varsigma} \\ \frac{c}{\varsigma} & \frac{-a}{\varsigma} & \frac{cs}{\varsigma} & -\frac{as}{\varsigma} \end{pmatrix} \tag{A.4}$$

$$\mathrm{C}^{-3} = \begin{pmatrix} \frac{a+2\varsigma s}{\varsigma^2} & \frac{b}{\varsigma^2} & \frac{as+\varsigma s^2}{\varsigma^2} & \frac{bs}{\varsigma^2} \\ \frac{c}{\varsigma^2} & \frac{-1+2\varsigma s}{\varsigma^2} & \frac{cs}{\varsigma^2} & \frac{-as+\varsigma s^2}{\varsigma^2} \\ \frac{1+as}{\varsigma} & \frac{bs}{\varsigma} & \frac{s}{\varsigma} & 0 \\ \frac{cs}{\varsigma} & \frac{1-as}{\varsigma} & 0 & \frac{s}{\varsigma} \end{pmatrix} \tag{A.5}$$

Finally we present $e^{\mathbf{C}}$. First we note the definition of the matrix exponential:

$$e^{\mathbf{C}} = \sum_{k=0}^{\infty} \frac{1}{k!} \mathbf{C}^k \tag{A.6}$$

The matrix $\mathbf{C}$ has block structure of the form

$$\mathbf{C} = \begin{pmatrix} \mathbf{0} & \mathbf{I} \\ \frac{1}{s}\mathbf{A} & -\frac{1}{s}\mathbf{I} \end{pmatrix} \tag{A.7}$$

Thus any power of $\mathbf{C}$ will have a block structure with the same sized blocks, with each block being a polynomial of $\mathbf{A}$. However, $\mathbf{A}$ is a 2×2 matrix. The Cayley-Hamilton theorem [32] states that any $n \times n$ matrix satisfies its own characteristic polynomial. As a result we can express $\mathbf{A}^2$ in terms of $\mathbf{I}$ and $\mathbf{A}$ which means that the highest power of $\mathbf{A}$ that can occur in the matrix exponential is $\mathbf{A}$. Hence we can form an ansatz

$$e^{\mathbf{C}} = \begin{pmatrix} f_1\mathbf{I} + f_2\mathbf{A} & f_3\mathbf{I} + f_4\mathbf{A} \\ f_5\mathbf{I} + f_6\mathbf{A} & f_7\mathbf{I} + f_8\mathbf{A} \end{pmatrix} \tag{A.8}$$

Matrix exponents in the exponential integration algorithm always occur as a product between a matrix such as $\mathbf{C}$ and a constant p. We expect the constant to only affect the coefficients $f_1, f_2, \ldots, f_8$ so we use the same kind of ansatz

$$e^{p\mathbf{C}} = \begin{pmatrix} f_1\mathbf{I} + f_2\mathbf{A} & f_3\mathbf{I} + f_4\mathbf{A} \\ f_5\mathbf{I} + f_6\mathbf{A} & f_7\mathbf{I} + f_8\mathbf{A} \end{pmatrix} \tag{A.9}$$

Let $d = \sqrt{a^2 + bc}$. We get two cases. If $d = i|d|$ is a pure complex number we define $z = \sqrt{1 + 16s^2|d|^2}$, $R = \frac{|p|}{2s}\sqrt{\frac{z+1}{2}}$ and $J = \frac{|p|}{2s}\sqrt{\frac{z-1}{2}}$ which then can be used to define $cc = \cosh(R)\cos(J)$, $ss = \sinh(R)\sin(J)$, $cs = \cosh(R)\sin(J)$ and $sc = \sinh(R)\cos(J)$. Then the coefficients are given by

$$\begin{aligned}
f_1 &= \frac{e^{-\frac{p}{2s}}}{2}\left(2 \cdot cc + \frac{p}{s(R^2+J^2)}(R \cdot sc + J \cdot cs)\right) \\
f_2 &= \frac{e^{-\frac{p}{2s}}}{2|d|}\left(2 \cdot ss + \frac{p}{s(R^2+J^2)}(-J \cdot sc + R \cdot cs)\right) \\
f_3 &= \frac{pe^{-\frac{p}{2s}}}{R^2+J^2}(R \cdot sc + J \cdot cs) \\
f_4 &= \frac{pe^{-\frac{p}{2s}}}{|d|(R^2+J^2)}(-J \cdot sc + R \cdot cs)) \\
f_5 &= \frac{p|d|e^{-\frac{p}{2s}}}{s(R^2+J^2)}(J \cdot sc - R \cdot cs) \\
f_6 &= \frac{pe^{-\frac{p}{2s}}}{s(R^2+J^2)}(R \cdot sc + J \cdot cs) \\
f_7 &= \frac{e^{-\frac{p}{2s}}}{2}\left(2 \cdot cc - \frac{p}{s(R^2+J^2)}(R \cdot sc + J \cdot cs)\right) \\
f_8 &= \frac{e^{-\frac{p}{2s}}}{2|d|}\left(2 \cdot ss - \frac{p}{s(R^2+J^2)}(-J \cdot sc + R \cdot cs)\right)
\end{aligned}$$

If on the other hand d is real we define $x = \frac{|p|}{2s}\sqrt{1+4ds}$ and get a condition on the sign of $\upsilon = 1 - 4ds$.

1. If $\upsilon > 0$ we define $y = \frac{|p|}{2s}\sqrt{\upsilon}$ and then define $ccp = \cosh(x) + \cosh(y)$, $ccm = \cosh(x) - \cosh(y)$, $ssp = \frac{\sinh(x)}{x} + \frac{\sinh(y)}{y}$ and $ssy = \frac{\sinh(x)}{x} - \frac{\sinh(y)}{y}$
2. If $\upsilon < 0$ we define $y = \frac{|p|}{2s}\sqrt{-\upsilon}$ and then define $ccp = \cosh(x) + \cos(y)$, $ccm = \cosh(x) - \cos(y)$, $ssp = \frac{\sinh(x)}{x} + \frac{\sin(y)}{y}$ and $ssy = \frac{\sinh(x)}{x} - \frac{\sin(y)}{y}$

In both cases the coefficients are then given by

$$
\begin{aligned}
f_1 &= \frac{e^{-\frac{p}{2s}}}{2}\left(ccp + \frac{p}{2s}ssp\right) \\
f_2 &= \frac{e^{-\frac{p}{2s}}}{2d}\left(ccm + \frac{p}{2s}ssm\right) \\
f_3 &= \frac{pe^{-\frac{p}{2s}}}{2}ssp \\
f_4 &= \frac{pe^{-\frac{p}{2s}}}{2d}ssm \\
f_5 &= \frac{pde^{-\frac{p}{2s}}}{2s}ssm \\
f_6 &= \frac{pe^{-\frac{p}{2s}}}{2s}ssp \\
f_7 &= \frac{e^{-\frac{p}{2s}}}{2}\left(ccp - \frac{p}{2s}ssp\right) \\
f_8 &= \frac{e^{-\frac{p}{2s}}}{2d}\left(ccm - \frac{p}{2s}ssm\right)
\end{aligned}
$$

B

The Probability Density Function of a Product of Gaussians

B.1 Bessel Functions

See [33, 34] for further details. Let us consider a differential equation of the form

$$\frac{d^2u}{dz^2}(z) + \frac{1}{z}\frac{du}{dz}(z) + \left(1 - \frac{\nu^2}{z^2}\right) u(z) = 0 \tag{B.1}$$

The solution to this differential equation is called the Bessel function of the first kind and has a power series representation

$$J_\nu(z) := \sum_{k=0}^{\infty} \frac{(-1)^k}{\Gamma(k+1)\Gamma(k+\nu+1)} \left(\frac{z}{2}\right)^{2k+\nu} \tag{B.2}$$

Here z is a complex variable and $\Gamma(\cdot)$ denotes the Gamma function. The parameter ν appearing in Eqs. (B.1) and (B.2) can take either real or complex values and represents the order of the Bessel function.
The modified Bessel functions of the first and second kind are defined by

$$I_\nu(z) := \sum_{k=0}^{\infty} \frac{1}{\Gamma(k+1)\Gamma(k+\nu+1)} \left(\frac{z}{2}\right)^{2k+\nu} \tag{B.3}$$

$$K_\nu(z) := \frac{\pi}{2}\frac{I_{-\nu}(z) - I_\nu(z)}{sin(\nu\pi)} \tag{B.4}$$

with $\nu \in \mathbb{R}$ and $z \in \mathbb{C}$. Note that $K_\nu(z)$ is undefined for integer values of ν so in this case we define it as a limit:

$$K_n(z) := \lim_{\nu \to n} K_\nu(z) \tag{B.5}$$

An integral representation can be obtained (cite Abramowitz and Stegun, Handbook of mathematical functions). For $z \in \mathbb{C}, |\arg(z)| < \pi/2$ we get

$$K_\nu(z) = \int_0^\infty e^{-z\cosh(t)} \cosh(\nu t) dt \tag{B.6}$$

For order 0, with a real and positive argument $x \in \mathbb{R}, x > 0$, this expression can be simplified to

$$K_0(x) = \int_0^\infty \cos(x\sinh(t)) dt = \int_0^\infty \frac{\cos(xt)}{\sqrt{t^2+1}} dt \tag{B.7}$$

B.2 The M = 1 Case

We want to find the probability density function of the product of two independent Gaussian random variables. Assume we have $X = cu$ where c and u are independent zero mean Gaussian random variables with variances σ_c^2 and σ_u^2. In that case their joint probability density function is

$$f(c,u) = \frac{1}{2\pi\sigma_c\sigma_u} e^{-\frac{c^2}{2\sigma_c^2}} e^{-\frac{u^2}{2\sigma_u^2}} \tag{B.8}$$

We can find the joint probability density function of X and u as

$$f(X,u) = f(c,u)\left|\frac{\partial c}{\partial X}\right| \tag{B.9}$$

Then the probability density function for X is

$$\begin{aligned} f(X) &= \int_{-\infty}^{\infty} f(X,u)du \\ &= \frac{1}{2\pi\sigma_c\sigma_u}\int_{-\infty}^{\infty}\frac{1}{|u|} e^{-\frac{X^2}{2\sigma_c^2u^2}} e^{-\frac{u^2}{2\sigma_u^2}} du \end{aligned}$$

The software Mathematica can be used to solve this integral, which yields

$$f(X) = \frac{1}{\pi\sigma_c\sigma_u} K_0\left(\frac{|X|}{\sigma_u\sigma_c}\right) \tag{B.10}$$

B.3 The M = 2 Case

Now assume we have $X = c_1u_1 + c_2u_2$ where c_1, u_1, c_2, u_2 are independent zero mean Gaussians where c_1 and c_2 have variance σ_c^2 and u_1 and u_2 have variance σ_u^2. Notice that we can write $c_1 = (X - c_2u_2)/u_1$. The joint probability density function is

$$f(c_1,c_2,u_1,u_2) = \frac{1}{(2\pi)^2\sigma_u^2\sigma_c^2} e^{-\frac{c_1^2}{2\sigma_c^2}-\frac{c_2^2}{2\sigma_c^2}-\frac{u_1^2}{2\sigma_u^2}-\frac{u_2^2}{2\sigma_u^2}} \tag{B.11}$$

and with the relation

$$f(X,c_2,u_1,u_2) = f(c_1,c_2,u_1,u_2)\left|\frac{\partial c_1}{\partial X}\right| \tag{B.12}$$

we find (letting $\gamma = 1/((2\pi)^2\sigma_u^2\sigma_c^2)$)

$$\begin{aligned} f(X) &= \int_{-\infty}^{\infty}\int_{-\infty}^{\infty}\int_{-\infty}^{\infty} f(X,c_2,u_1,u_2)dc_2du_1du_2 \\ &= \gamma\int_{-\infty}^{\infty}\int_{-\infty}^{\infty}\int_{-\infty}^{\infty}\frac{1}{|u_1|} e^{-\frac{(X-c_2u_2)^2}{2\sigma_c^2u_1^2}} e^{-\frac{c_2^2}{2\sigma_c^2}} e^{-\frac{u_1^2}{2\sigma_u^2}} e^{-\frac{u_2^2}{2\sigma_u^2}} dc_2du_1du_2 \end{aligned}$$

The integral with respect to u_2 can now be evaluated with Mathematica, resulting in (hereafter the limits of the integrals are omitted if they span $-\infty$ to ∞)

$$f(X) = \sqrt{2\pi}\gamma \int\int \frac{1}{\sqrt{\frac{c_2^2}{\sigma_c^2} + \frac{u_1^2}{\sigma_u^2}}} e^{-\frac{1}{2}\left(\frac{c_2^2}{\sigma_c^2} + \frac{u_1^2}{\sigma_u^2} + \frac{X^2}{c_2^2\sigma_u^2 + u_1^2\sigma_c^2}\right)} dc_2 du_1$$

Now the following variable substitution is done

$$u_1' = \frac{u_1}{\sigma_u} \tag{B.13}$$

$$c_2' = \frac{c_2}{\sigma_c} \tag{B.14}$$

$$(X')^2 = \frac{X^2}{\sigma_u^2\sigma_c^2} \tag{B.15}$$

Then the integral simplifies to

$$f(X) = \sqrt{2\pi}\sigma_u\sigma_c\gamma \int\int \frac{1}{\sqrt{(c_2')^2 + (u_1')^2}} e^{-\frac{1}{2}\left((c_2')^2 + (u_1')^2 + \frac{(X')^2}{(c_2')^2 + (u_1')^2}\right)} dc_2' du_1'$$

Now substitution to polar coordinates $r = \sqrt{(c_2')^2 + (u_1')^2}$ yields (the angular integral constitutes a factor of 2π)

$$\begin{aligned} f(X) &= \gamma\sigma_u\sigma_c(2\pi)^{3/2} \int_0^\infty \frac{1}{r} e^{-\frac{1}{2}\left(r^2 + \frac{(X')^2}{r^2}\right)} r dr \\ &= \gamma\sigma_u\sigma_c(2\pi)^{3/2} \int_0^\infty e^{-\frac{1}{2}\left(r^2 + \frac{(X')^2}{r^2}\right)} dr \\ &= 2\pi^2\gamma\sigma_u\sigma_c e^{-|X'|} \end{aligned}$$

Where the last integral was evaluated using Mathematica. Putting back in the values for γ and X' we finally end up with

$$f(X) = \frac{1}{2\sigma_u\sigma_c} e^{-\frac{|X|}{\sigma_u\sigma_c}} \tag{B.16}$$

B.4 The M = 3 Case

The final case we are interested in is where X is the sum of three Gaussian products. Let us write $X = c_1u_1 + c_2u_2 + c_3u_3$ with $c_1, u_1, c_2, u_2, c_3, u_3$ independent zero mean Gaussians where c_1, c_2 and c_3 have variance σ_c^2 and u_1, u_2 and u_3 have variance σ_u^2. The joint probability density function is

$$f(c_1, c_2, c_3, u_1, u_2, u_3) = \frac{1}{(2\pi)\sigma_c^3\sigma_u^3} e^{-\frac{1}{2}\left(\frac{c_1^2 + c_2^2 + c_3^2}{2\sigma_c^2} + \frac{u_1^2 + u_2^2 + u_3^2}{2\sigma_u^2}\right)} \tag{B.17}$$

and

$$f(X, c_2, c_3, u_1, u_2, u_3) = f(c_1, c_2, c_3, u_1, u_2, u_3) \left|\frac{\partial c_1}{\partial X}\right| \tag{B.18}$$

Now denoting $\gamma = 1/((2\pi)^3\sigma_u^3\sigma_c^3)$ and writing integrals from $-\infty$ to ∞ without their limits we get

$$f(X) = \gamma \int\int\int\int\int \frac{1}{|u_1|} e^{-\frac{1}{2}\left(\frac{(X-c_2u_2-c_3u_3)^2}{u1_2\sigma_c^2}\right)} \tag{B.19}$$

$$e^{-\frac{1}{2}\left(\frac{c_2^2+c_3^2}{2\sigma_c^2}+\frac{u_1^2+u_2^2+u_3^2}{2\sigma_u^2}\right)} dc_2dc_3du_1du_2du_3 \tag{B.20}$$

Mathematica can now be used to evaluate the integral over u_3, yielding

$$f(X) = \sqrt{2\pi}\gamma \int\int\int\int \frac{1}{\sqrt{\frac{u_1^2}{\sigma_u^2}+\frac{c_3^2}{\sigma_c^2}}} e^{-\frac{c_3^4\sigma_u^4+\sigma_c^4u_1^4+\sigma_c^4u_q^2u_2^2}{2\sigma_c^2\sigma_u^2(c_3^2\sigma_u^2+\sigma_c^2u_1^2)}}$$
$$e^{-\frac{c_3\sigma_c^2\sigma_u^2(2u_1^2+u_2^2)+c_2^2(c_3^2\sigma_u^4+\sigma_c^2\sigma_u^2(u_1^2+u_2^2))}{2\sigma_c^2\sigma_u^2(c_3^2\sigma_u^2+\sigma_c^2u_1^2)}}$$
$$e^{\frac{2c_2\sigma_c^2\sigma_u^2u_2X-\sigma_c^2\sigma_u^2X^2}{2\sigma_c^2\sigma_u^2(c_3^2\sigma_u^2+\sigma_c^2u_1^2)}} dc_2dc_3du_1du_2$$

We now do a substitution

$$u_1' = \frac{u_1}{\sigma_u} \qquad u_2' = \frac{u_2}{\sigma_u} \tag{B.21}$$

$$c_2' = \frac{c_2}{\sigma_c} \qquad c_3' = \frac{c_3}{\sigma_u} \tag{B.22}$$

and after some simplification we get (we omit primes)

$$f(X) = \sqrt{2\pi}\gamma\sigma_u^2\sigma_c^2 \int\int\int\int \frac{1}{\sqrt{u_1^2+c_3^2}} e^{-\frac{u_2^2+c_2^2}{2}} e^{-\frac{u_1^2+c_3^2}{2}}$$
$$e^{-\frac{1}{2(u_1^2+c_3^2)}\left(\frac{X}{\sigma_u\sigma_c}-c_2u_2\right)} dc_2dc_3du_1du_2$$

Once again Mathematica can be used to evaluate the integral over c_2 which yields, after some simplification,

$$f(X) = 2\pi\gamma\sigma_u^2\sigma_c^2 \int\int\int \frac{1}{\sqrt{u_1^2+u_2^2+c_3^2}} e^{-\frac{c_3^2+u_1^2+u_2^2}{2}} e^{-\frac{X^2/(\sigma_u^2\sigma_c^2)}{2(c_3^2+u_1^2+u_2^2)}} du_1du_2dc_3$$

Doing a coordinate change to spherical coordinates gives

$$\begin{aligned} f(X) &= 2\pi\gamma\sigma_u^2\sigma_c^2 \int\int\int \frac{1}{r} e^{-\frac{r^2}{2}} e^{-\frac{X^2/(\sigma_u^2\sigma_c^2)}{2r^2}} r^2\sin(\theta) dr d\theta d\varphi \\ &= 8\pi^2\gamma\sigma_u^2\sigma_c^2 \int re^{-\frac{r^2}{2}} e^{-\frac{X^2/(\sigma_u^2\sigma_c^2)}{2r^2}} dr \\ &= 8\pi^2\gamma\sigma_u^2\sigma_c^2 \frac{|X|}{\sigma_u\sigma_c} K_1\left(\frac{|X|}{\sigma_u\sigma_c}\right) \end{aligned}$$

where the final integral was evaluated using Mathematica. Now putting back the value for γ we get

$$f(X) = \frac{|X|}{\pi\sigma_u^2\sigma_c^2} K_1\left(\frac{|X|}{\sigma_u\sigma_c}\right) \tag{B.23}$$

C

Integration Schemes

Here we present the integration schemes utilised during the course of this research. In all cases we solve an initial value problem of the form

$$\frac{dz}{dt}(t) = Lz(t) + N(t, z(t)) \tag{C.1}$$
$$z(0) = z_0 \tag{C.2}$$

The timestep h is used, and we write $f(t, z) = Lz + N(t, z)$ in section C.1. The notation f_n refers to the function value at time t_n, $f_n = f(t_n, z(t_n))$, and t_n denotes the time after n timesteps, $t_n = t_0 + nh$. More information about the exponential integration schemes can be found in [26, 27] and for the other schemes in [35].

C.1 Common Integrators

C.1.1 Forward Euler

$$z_{n+1} = z_n + hf(t_n, z_n) \tag{C.3}$$

C.1.2 Second order Runge-Kutta, RK2

$$z_m = z_n + \frac{h}{2} f(t_n, z_n) \tag{C.4a}$$
$$z_{n+1} = z_n + hf(t_n + \frac{h}{2}, z_m) \tag{C.4b}$$

C.1.3 Fourth order Runge-Kutta, RK4

$$k1 = f(t_n, z_n) \tag{C.5a}$$
$$k2 = f(t_n + \frac{h}{2}, z_n + k_1 \frac{h}{2}) \tag{C.5b}$$
$$k3 = f(t_n + \frac{h}{2}, z_n + k_2 \frac{h}{2}) \tag{C.5c}$$
$$k4 = f(t_n + h, z_n + k_3 h) \tag{C.5d}$$
$$z_{n+1} = z_n + \frac{h}{6}(k_1 + 2k_2 + 2k_3 + k_4) \tag{C.5e}$$

C.2 Exponential Integrators

C.2.1 First Order Exponential Time Differencing, ETD

$$z_{n+1} = e^{Lh} z_n + L^{-1}(e^{Lh} - I)N(t_n, z_n) \tag{C.6}$$

C.2.2 First order Integrating Factor Method, IF

$$z_{n+1} = e^{Lh}(z_n + hN(t_n, z_n)) \tag{C.7}$$

C.2.3 RK2 Based ETD, RK2ETD

$$\begin{aligned} z_m &= e^{Lh/2} z_n + L^{-1}(e^{Lh/2} - I)N(t_n, z_n) && \text{(C.8a)} \\ z_{n+1} &= e^{Lh} z_n + L^{-1}(e^{Lh} - I)N(t_n, z_n) + \\ &\quad \frac{2}{h} L^{-2}(e^{Lh} - I - Lh)(N(t_n + \frac{h}{2}, z_m) - N(t_n, z_n)) && \text{(C.8b)} \end{aligned}$$

C.2.4 RK2 Based IF method, RK2IF

$$\begin{aligned} z_m &= e^{Lh/2}(z_n + N(t_n, z_n)\frac{h}{2}) && \text{(C.9a)} \\ z_{n+1} &= e^{Lh} z_n + h e^{Lh/2} N(t_n + \frac{h}{2}, z_m) && \text{(C.9b)} \end{aligned}$$

C.2.5 RK4 Based ETD, RK4ETD

$$\begin{aligned} a_n &= e^{Lh/2} z_n + L^{-1}(e^{Lh/2} - 1)N(t_n, z_n) && \text{(C.10a)} \\ b_n &= e^{Lh/2} z_n + L^{-1}(e^{Lh/2} - 1)N(t_n + h/2, a_n) && \text{(C.10b)} \\ c_n &= e^{Lh/2} a_n + L^{-1}(e^{Lh/2} - 1)(2N(t_n + h/2, b_n) - N(t_n, z_n)) && \text{(C.10c)} \\ z_{n+1} &= e^{Lh} z_n + \frac{1}{h^2} L^{-3}\{[-4 - hL + e^{Lh}(4 - 3hL + h^2L^2)]N(t_n, z_n) \\ &\quad 2[2 + hL + e^{Lh}(-2 + hL)](N(t_n + h/2, a_n) + N(t_n + h/2, b_n)) \\ &\quad [-4 - 3hL - h^2L^2 + e^{Lh}(4 - hL)]N(t_n + h, c_n)\} && \text{(C.10d)} \end{aligned}$$

DEPARTMENT OF MATHEMATICS
CHALMERS UNIVERSITY OF TECHNOLOGY
Gothenburg, Sweden
www.chalmers.se

CHALMERS
UNIVERSITY OF TECHNOLOGY